Monthly Notices
of the
ROYAL ASTRONOMICAL SOCIETY

MNRAS **468,** 3663–3681 (2017)
Advance Access publication 2017 March 23

doi:10.1093/mnras/stx718

Super-Eddington QSO RX J0439.6−5311 – I. Origin of the soft X-ray excess and structure of the inner accretion flow

Chichuan Jin,[1]★ Chris Done[2] and Martin Ward[2]

[1]*Max-Planck-Institut für Extraterrestrische Physik, Giessenbachstrasse, D-85748 Garching, Germany*
[2]*Centre for Extragalactic Astronomy, Department of Physics, University of Durham, South Road, Durham DH1 3LE, UK*

Accepted 2017 March 21. Received 2017 March 20; in original form 2017 January 4

ABSTRACT

We report the results from a recent 133 ks *XMM–Newton* observation of a highly super-Eddington narrow-line Type-1 quasi-stellar object RX J0439.6−5311. This source has one of the steepest active galactic nuclei hard X-ray slopes, in addition to a prominent and smooth soft X-ray excess. Strong variations are found throughout the 0.3–10 keV energy range on all time-scales covered by the observation, with the soft excess mainly showing low-frequency (LF) variations below 0.1 mHz while the hard X-rays show stronger variability at higher frequencies. We perform a full set of spectral-timing analysis on the X-ray data, including a simultaneous modelling of the time-averaged spectra, frequency-dependent root-mean-square and covariance spectra, lag-frequency and lag-energy spectra. Especially, we find a significant time-lag signal in the LF band, which indicates that the soft X-rays lead the hard by ∼4 ks, with a broad continuum-like profile in the lag spectrum. Our analysis strongly supports the model where the soft X-ray excess is dominated by a separate low temperature, optically thick Comptonization component rather than relativistic reflection or a jet. This soft X-ray emitting region is several tens or hundreds of R_g away from the hot corona emitting hard X-rays, and is probably associated with a geometrically thick ('puffed-up') inner disc region.

Key words: accretion, accretion discs – galaxies: active – galaxies: nuclei.

1 INTRODUCTION

Narrow-line Seyfert 1 (NLS1) galaxies are an intriguing subclass of active galactic nuclei (AGN, Osterbrock & Pogge 1985; Boroson & Green 1992), consistent on average with having lower black hole masses and higher mass accretion rates compared with typical Seyfert 1s. They typically have steep 2–10 keV spectra (Brandt, Mathur & Elvis 1997), and even steeper spectra at lower energies forming a prominent soft X-ray excess below ∼2 keV (e.g. Boller, Brandt & Fink 1996; Leighly 1999; Boroson 2002). Gallo (2006) proposed that NLS1s could be split into two types. There are 'complex' NLS1s that show deep dips in their X-ray light curves, during which their hard X-ray spectra become harder and contain strong features around the Fe Kα line, and 'simple' NLS1s that do not show these features. So far the most robust AGN quasi-periodic oscillation (QPO) detection is also in the 'simple' NLS1 RE J1034+396 (Gierliński et al. 2008; Alston et al. 2014b).

While there is general consensus that the high-energy 2–10 keV emission in AGN is from the Compton up-scattering by high temperature, optically thin electrons in a corona, the origin of the soft X-ray excess is less clear. There are two main models proposed for this, namely the highly relativistically smeared, partially ionized reflection model (e.g. Miniutti & Fabian 2004; Fabian & Miniutti 2005; Ross & Fabian 2005; Crummy et al. 2006), and the low temperature, optically thick Comptonization model (Laor et al. 1997; Magdziarz et al. 1998; Gierliński & Done 2004; Mehdipour et al. 2011; Done et al. 2012). Both models can fit the spectra equally well over the classic 0.3–10 keV X-ray bandpass, and both require some fine-tuning of parameters: Comptonization models all give very similar temperatures (Czerny et al. 2003; Gierliński & Done 2004; Porquet et al. 2004) while reflection models give similar ionization states (Done & Nayakshin 2007).

None the less, the models can be separated with variability or higher energy data. Noda et al. (2011) use the fast variability in the broad-line Seyfert 1 (BLS1) Mkn 509 to show that on the shortest time-scales there is a constant component in the spectrum which has a shape compatible with thermal Comptonization and not with reflection. Similarly, including high-energy data shows that a thermal Comptonization component is better than reflection in terms of fitting the soft X-ray excess in BLS1s (Boissay et al. 2014; Matt et al. 2014; Mehdipour et al. 2015). Lohfink et al. (2016) similarly find the soft X-ray excess in the BLS1 Fairall 9 is dominated by an additional component (though they model it with a very steep power law rather than thermal Comptonization). They also require some additional relativistically smeared reflection, but this

★ E-mail: chichuan@mpe.mpg.de

disappears when more physical models are used to describe the narrow torus reflection component in these data (Yaqoob et al. 2016). Thus, in BLS1s there is mounting evidence that the soft X-ray excess is an additional thermal Comptonization component.

However, in NLS1s the situation is more open. The key observation is that the new spectral-timing techniques reveal a soft lag in the data, consistent with the reflection geometry as reflected photons have longer light paths than those from the hot corona. This predicts a reverberation time lag for the reflected emission which depends on the height of the corona and the black hole mass (Fabian et al. 2009, 2013, 2014; Zoghbi et al. 2010; Zoghbi & Fabian 2011; Zoghbi, Uttley & Fabian 2011; Kara et al. 2013a,b,c; Uttley et al. 2014; Chiang et al. 2015). While the reflected spectrum is dominated by the iron line in the 6–7 keV bandpass, this reverberation lag is as strong or stronger at soft energies for partially ionized reflection, and current instruments have so much more effective area below 2 keV that this is much easier to detect as a soft lag than as an iron line lag (though the latter R_{sx} has also been seen: De Marco et al. 2013; Kara et al. 2016).

However, the reflection-dominated model often requires extreme parameters, with the X-ray source being very close to the event horizon of a high spin black hole. This is inconsistent with the lag-frequency spectra seen from these objects, as these are actually dominated by a soft lead at low frequencies, which only switches to the reverberation soft lag for the fastest variability time-scales (e.g. Alston, Done & Vaughan 2014a; Jin, Done & Ward 2016). A soft lead on time-scales much longer than the soft lags requires that the hard X-rays respond to changes in the soft X-ray flux on time-scales which are longer than the light traveltime between the two regions. These longer lags are generally interpreted as propagation, where fluctuations in the accretion flow propagate down to progressively smaller radii which emit harder spectra (e.g. Lyubarskii 1997; Kotov, Churazov & Gilfanov 2001). This is most naturally produced in a radially stratified flow, which requires that a large fraction of the soft X-ray excess is intrinsically produced in the flow rather than being reflected (but see Chainakun & Young 2017 for an alternative dual lamppost model).

Thus, it seems most likely that in NLS1s there is a mix of both intrinsic (soft leads) and reprocessed (soft lags) emission making up the soft X-ray excess. Gardner & Done (2014) do a full spectral-timing model and find that they can model the lag-frequency spectrum in the 'simple' NLS1 PG 1244+026 by a model where fluctuations in the thermal Comptonization inner disc region propagate down to the high-energy corona. The high-energy X-rays reflect from the same inner disc, producing a small, moderately (not extremely) smeared reflection component. This is not sufficient to produce the observed soft lag, but many of the illuminating photons are not reflected, so instead are absorbed in the disc. These should thermalize, producing a (quasi) blackbody soft component that reverberates with the harder X-rays, producing the observed lag. This model can also be generalized to fit the much shorter observed soft lag of a few tens of seconds seen in the 'complex' NLS1s if much of the extreme variability is associated with occultation events (Gardner & Done 2015).

Both 'simple' and 'complex' NLS1s may well be accreting at super-Eddington rates (Done & Jin 2016), in which case the occultations can easily be explained as arising from the clumpy disc wind that should be produced at such mass accretion rates (Ohsuga & Mineshige 2011; Jiang et al. 2014; Takeuchi et al. 2014; Done & Jin 2016; Hagino et al. 2016). This also provides a way to unify the 'simple' and 'complex' NLS1s if the differences in their X-ray spectra and variability are caused by differences in the viewing angle relative to the clumpy wind. We note that complex absorption has long been suggested as the origin of the extreme iron features associated with the 'complex' NLS1s (Miller et al. 2007; Turner et al. 2007; Sim et al. 2010; Tatum et al. 2012).

The number of NLS1s that are bright enough and/or have long enough observations to allow a detailed spectral-timing analysis is very limited. Here, we present the analysis of a recent 133 ks *XMM–Newton* observation of another 'simple' NLS1, namely RX J0439.6−5311. This source is a relatively nearby, Type-1 narrow-line quasi-stellar object (QSO) ($z = 0.243$, Thomas et al. 1998), with a Galactic gas column density of $N_{\rm H} = 7.45 \times 10^{19}$ cm^{-2} (Kalberla et al. 2005) and no significant intrinsic extinction (Grupe et al. 2010), indicating a very clear line of sight. The H β full width at half-maximum of RX J0439.6−5311 was found to be only 700 ± 140 km s^{-1}, which is the narrowest among all the 110 soft X-ray selected AGN in Grupe et al. (2004, also see Bian & Zhao 2004). Based on the *Swift* observation, Grupe et al. (2010) report a soft X-ray slope of ∼2.2, a single-epoch black hole mass of 3.9×10^6 M$_\odot$ and an extreme Eddington ratio of 12.9 that is derived from the broad-band spectral energy distribution. Therefore, RX J0439.6−5311 has a very similar X-ray spectral shape to the 'simple' NLS1s such as PG 1244+026 and RE J1034+396, but with an even more extreme mass accretion rate, potential more comparable to 1H 0707−495 (Done & Jin 2016). The study of this source allows us to further understand the soft excess mechanism in these unobscured, highly accreting AGN, and to identify additional ubiquitous properties among these sources.

This paper is organized as follows. First, we describe the latest *XMM–Newton* observation of RX J0439.6−5311 and our data reduction procedures. Then we present the source's variability properties in Section 3. A detailed spectral-timing modelling is present in Section 4, in order to separate the various components and to understand their origins. In Section 5, we report results from our X-ray interband coherence and covariance analysis. The interband time-lag analysis is present in Section 6. Discussion of the soft X-ray excess and its potential connection with the region of inner disc which we claim is puffed up, is given in Section 7. Finally, Section 8 summaries the main results of this work. We adopt a flat universe model for the luminosity distance with the Hubble constant $H_0 = 72$ km s^{-1} Mpc^{-1}, $\Omega_\Lambda = 0.73$ and $\Omega_{\rm M} = 0.27$.

2 *XMM–NEWTON* OBSERVATION AND DATA REDUCTION

XMM–Newton (Jansen et al. 2001) observed RX J0439.6−5311 on 2016-02-12 for a continuous duration of 133 ks (PI: C. Jin). All three European Photon Imaging Cameras (EPIC; pn, MOS1, MOS2) were operated in the *Imaging* data-mode, with the EPIC-pn camera in the *PrimeLargeWindow* mode with the *thick* filter, and the two MOS cameras in the *PrimePartialW3* mode with the *thin* filter. The two reflection grating spectrometer (RGS) cameras were both in the *Spectroscopy* data-mode. The optical monitor (OM) was in the *Imaging+Fast* data-mode with exposures in six optical/UV filters (*V*, *B*, *U*, *UVW*1, *UVM*2, *UVW*2).

We followed the standard procedures of using the SAS software (v15.0.0) and the latest calibration files to reduce the data. The `epproc` and `emproc` tasks were used to reprocess the EPIC data and create the event files. The `rgsproc` and `omfchain` tasks were used to reprocess the RGS and OM data. For the EPIC data, we defined a source extraction region of 80 arcsec centred at the position of RX J0439.6−5311, and extracted background from a nearby

region of the same size without any point source contamination. By checking the background light curve above 12 keV, we found that this observation is almost free from high background flares except for some short periods at the beginning and end of the exposure. As a result we excluded all contaminated data from the first 4 ks and last 8 ks using the `tabgtigen` task. The filtered observation has a continuous 121 ks duration with 113 ks exposure in EPIC-pn (94.9 per cent live time) and 120 ks exposure in MOS1 and MOS2 (99.5 per cent live time). The background subtracted mean source count rates are 2.01 counts per second (cps), 0.64 cps and 0.61 cps in EPIC-pn, MOS1 and MOS2, respectively, which are all well below the pile-up threshold for the chosen observing mode and filter. We further checked that there is no photon pile-up in any of the three EPIC cameras by running the `epatplot` task.[1] In the subsequent analysis, we only adopted good events (FLAG=0) with PATTERN ≤ 4 for EPIC-pn (i.e. single and double patterns) and PATTERN ≤ 12 for MOS1 and MOS2 (i.e. single, double, triple, quadruple patterns).[2]

The EPIC light curves and spectra were extracted from the source and background regions separately using the `evselect` task. These regions were chosen to avoid the CCD area where the copper instrumental background is high (Freyberg et al. 2004). The `epiclccorr` task was used to perform the background subtraction and *Absolute* corrections on the source light curves for various instrumental factors. The `rmgfen`, `arfgen` and `backscale` tasks were used to create response and auxiliary files and to calculate the scaling factor. The RGS spectra were extracted using the `rgsproc` task. All the EPIC and RGS spectra were grouped with at least 20 counts per bin using the `grppha` tool (FTOOLS v6.19). Spectral fittings were performed using the XSPEC (v12.9.0u) package (Arnaud 1996).

3 X-RAY VARIABILITY ANALYSIS

Variability studies can provide crucial information concerning the mechanism of the soft X-ray emission and to help break the degeneracy of spectral components. This clean and uninterrupted 120 ks *XMM–Newton* observation of RX J0439.6−5311 reveals the characteristics of its energy-dependent variability in great detail.

3.1 EPIC light curves

We first compared the light curves extracted from the 0.3–1, 1–2 and 2–10 keV bands. After applying all the filtering, correction and background subtraction (see Section 2), the intrinsic source variability can be visualized in these light curves. Fig. 1 shows that RX J0439.6−5311 exhibits strong variability in all three X-ray bands. The count rate varies by ±50 per cent over tens of ks. For time-scales of ks and shorter, the 2–10 keV band shows a factor of 2 variability, while the 0.3–1 keV band is more stable on these short time-scales. This is confirmed by the intrinsic fractional root-mean-square (rms) variability (Edelson et al. 2002; Markowitz, Edelson & Vaughan 2003; Vaughan et al. 2003b), which is 22.4 ± 0.2 per cent, 28.7 ± 0.4 per cent, 47.5 ± 1.1 per cent for the 0.3–1, 1–2 and 2–10 keV bands, respectively.[3]

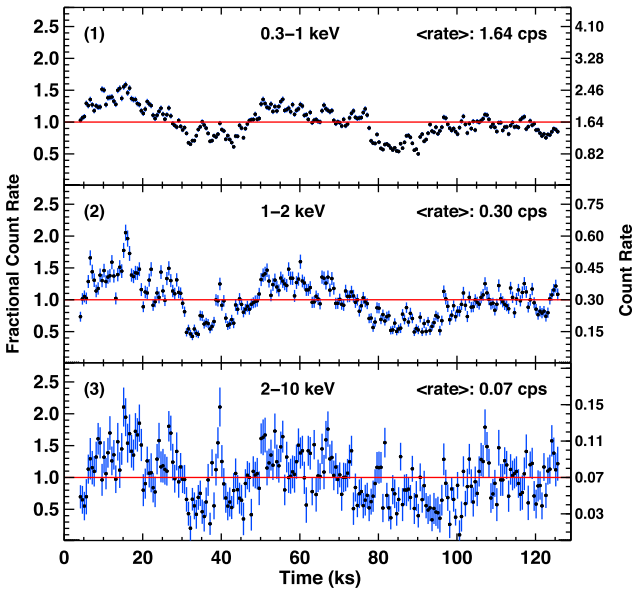

Figure 1. Light curves of RX J0439.6−5311 observed by the *XMM–Newton* EPIC-pn camera in the 0.3–1, 1–2 and 2–10 keV bands (background subtracted, binned with 500 s). The left *y*-axis is in the unit of fractional count rate relative to the mean count rates (<rate>), while the right *y*-axis is the absolute count rate. High background periods at the beginning and end of the observation have been masked out.

3.2 Power spectra density (PSD)

A PSD quantifies the variability power in different frequency bands. We first combined light curves from all three EPIC cameras to maximize the signal to noise (S/N) using the `lcmath` tool (FTOOLS v6.19), and then calculated the PSD from the combined light curve using the `powspec` tool. The normalization of `powspec` was chosen to be −2, which allowed it to produce a white noise subtracted PSD, the integration of which gives the excess variance. The resultant PSDs are binned with a geometrical step of 1.4 and plotted in Fig. 2.

These PSDs show significant variability across a wide frequency band (10^{-5}–10^{-3} Hz) covered by the *XMM–Newton* observation, extending from the soft up to the hard X-rays. There is no detection of periodic signals, which is not surprising as QPOs in AGN are very rare, and not always easy to detect even when present (Middleton et al. 2009; Alston et al. 2014b)

For the high-frequency (HF) band of $f \geq 10^{-4}$ Hz, the hard X-rays show stronger rms variability than seen in the soft X-rays. This is also observed in several other NLS1s of high mass accretion rates (e.g. PG 1244+026, Jin et al. 2013; RE J1034+396, Middleton et al. 2009; Ark 564, M^{c}Hardy et al. 2007). There is a HF rollover in the 0.3–1 keV band PSD (Fig. 2a). A broken power-law fit to the PSD indicates a best-fitting break frequency of $\nu_{\rm b} = 6.4^{+4.7}_{-2.7} \times 10^{-4}$ Hz (1σ confidence level, red dashed line in Fig. 2a). Assuming a power-law form of $P(f) \propto f^{\alpha}$, we

[1] In the *PrimeLargeWindow* mode, EPIC-pn has a 3 cps threshold for 2.5 per cent flux-loss. We noticed that the source count rate may exceed 3 cps slightly during short flaring peaks of the first 30 ks. As a double check for the pile-up effect, for the first 30 ks, we re-ran the SAS `epatplot` task and found no significant pile-up effect. We also compared the spectra before and after excluding the central 10 arcsec point spread function area and found no significant differences either, so we can conclude that pile-up should not affect our analysis.

[2] https://xmm-tools.cosmos.esa.int/external/xmm_user_support/documentation/uhb/epic_evgrades.html

[3] rms errors were calculated using equation B2 in Vaughan et al. (2003b).

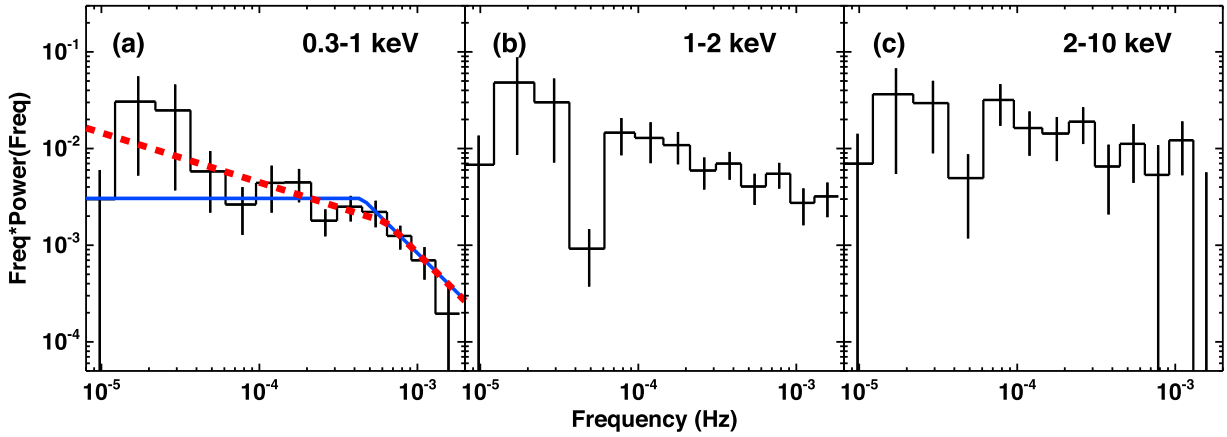

Figure 2. The PSD of RX J0439.6−5311 in various X-ray bands. These are produced by the POWSPEC tool (FTOOLS v6.19), with the Poisson noise subtracted, rebinned with a geometrical step of 1.4, and plotted in $f \cdot P(f)$ versus f. The normalization is chosen such that the integration of the PSD over a specific frequency band gives the fractional excess variance. In Panel a, the blue solid line and red dash line are two best-fitting broken power-law models. The blue line's slope is fixed at $\alpha = -1$ below the break frequency (see Section 3.2).

find $\alpha_1 = -1.51^{+0.19}_{-0.19}$ (the 90 per cent confidence range is [−1.81, −1.19]) and $\alpha_2 = -2.64^{+0.87}_{-1.36}$ below and above the break frequency. This indicates a similar PSD shape to some other NLS1s such as Ark 564 around the HF break (M^{c}Hardy et al. 2007). If the slope below the break frequency is fixed at −1, we find $\nu_b = 4.4^{+1.1}_{-4.4} \times 10^{-4}$ Hz (blue solid line in Fig. 2a) that is slightly lower than in the previous fit, with $\alpha_1 = -2.62^{+1.31}_{-0.70}$ that is consistent with the previous value. The S/N of PSDs of the higher energy bands is not sufficient to provide strong constraints on the broken power-law model.

3.3 Frequency-dependent rms spectra

The X-ray variability not only has an energy dependence, but also has a clear frequency dependence as already seen in the PSD. This can be revealed directly by the frequency-dependent rms spectra (Arévalo et al. 2008; Middleton et al. 2009; Jin et al. 2013, here after: J13). We adopted the prescription in Arévalo et al. (2008) to calculate the frequency-dependent rms from the PSD in every energy bin, and used the equations given in Poutanen, Zdziarski & Ibragimov (2008) to calculate the error. To reduce the number of zero-count bins in the light curve, which would otherwise bias the rms, we combined light curves from all three EPIC cameras and chose a binning time of 400 s. With careful division of energy bins, all the light curves below 4 keV have ≤5 zero-count bins out of 305 bins (i.e. <2 per cent), while the 4–6 keV light curve has 9 zero-count bins (3 per cent) and 6-8 keV light curve has 70 zero-count bins (23 per cent). The light curve above 8 keV has more than 50 per cent zero/negative-count bins after background subtraction, so we did not use it in the timing analysis. Each light curve has bins of 400 s and 120 ks long, which corresponds to a frequency range of 8.3×10^{-6}–1.25×10^{-3} Hz. Since the PSDs in Fig. 2 show the soft X-rays have smaller rms than the hard X-rays above 10^{-4} Hz, we chose to divide the frequency range into two sub-ranges at 10^{-4} Hz, and refer to $f \geq 1 \times 10^{-4}$ Hz as the HF band and $f < 1 \times 10^{-4}$ Hz as the low-frequency (LF) band.

Similar to other 'simple' NLS1s such as RX J0136.9−3510 (Jin et al. 2009), RE J1034+396 (Middleton et al. 2009), PG 1244+026 (J13) and RX J1140.1−0307 (Jin et al. 2016), the HF rms of RX J0439.6−5311 increases steeply from soft to hard X-rays, suggesting a strong dilution to the HF variability in the soft excess

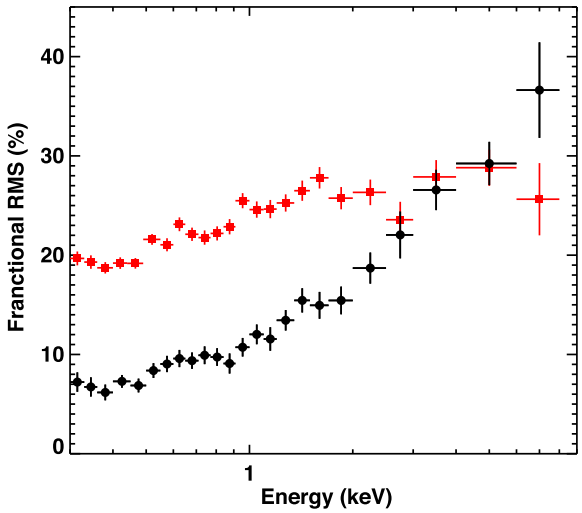

Figure 3. The energy-dependent rms fractional variability in the low-frequency band (8.3×10^{-6}–10^{-4} Hz, red square points) and high-frequency band (10^{-4}–1.25×10^{-3} Hz, black circular points).

(Fig. 3). The LF rms spectrum shows strong variability across the entire X-ray band with no obvious trend, which is different from PG 1244+026 where the LF rms was strongly suppressed in the hard X-ray band (J13), and also different from RE J1034+396 where the LF rms is small across the entire X-ray band (Middleton et al. 2009). These rms spectra imply that there must be at least two major X-ray components with different variability behaviours dominating the soft and hard X-ray bands separately, which we will model in the next section.

4 TIME-AVERAGED X-RAY SPECTRA

4.1 Epic spectra

Based on previous studies of similar NLS1s such as RE J1034+396 (Middleton et al. 2009) and PG 1244+026 (J13), we perform spectral fittings on the time-averaged spectra by employing two distinct physical scenarios, namely the Comptonization-dominated scenario (Laor et al. 1997) and the reflection-dominated scenario

(Fabian & Miniutti 2005). Some other models were also proposed in the literatures, such as the smeared absorption model (Gierliński & Done 2004, 2006; but see Schurch & Done 2007) and partial covering absorption model (Miller et al. 2007; Reeves et al. 2008; Sim et al. 2010; Tatum et al. 2012), but these models were less favoured by other similar NLS1s in terms of both spectral shape and variability grounds (Miniutti et al. 2009; Ai et al. 2011; J13).

To increase the spectral constraints, we fit all three EPIC spectra simultaneously, and adopt a free constant to account for their small normalization differences. In the EPIC-pn spectrum, we noticed some absorption features within 8–9 keV which was not found in the two MOS spectra, and was not found before the background subtraction, so these feature are likely caused by the subtraction Cu Kα instrumental background when the source count rate is too low above 8 keV, so we excluded the EPIC-pn data within 8–9 keV to avoid this background contamination. Galactic extinction along the line of sight to RX J0439.6−5311 is $N_{\rm H} = 7.45 \times 10^{-19}$ cm^{-2} (Kalberla et al. 2005), which is modelled with the TBNEW model in XSPEC using cross-sections of Verner et al. (1996) and the interstellar medium abundances of Wilms, Allen & McCray (2000). Host galaxy extinction is also modelled with TBNEW by setting the redshift to 0.243. In both the Comptonization and reflection scenarios, hard X-rays come from the Compton up-scattering of seed photons by electrons in the hot corona. We model this X-ray component with the NTHCOMP model (Zdziarski, Johnson & Magdziarz 1996) and fix the electron temperature at 100 keV (J13). Since RX J0439.6−5311 has a high mass accretion rate and a relatively low black hole mass, its accretion disc emission is probably hot enough to extend into the soft excess (Done et al. 2012, 2013; DJ16). Thus, we add a DISKBB model to the soft X-ray band. However, the disc and coronal power law are not sufficient to provide a good fit to the soft excess (Done et al. 2012), and so it requires another model component. Below we present the spectral fitting of Comptonization- and reflection-dominated models for the soft excess. Note that the physical mechanisms of these two models do not conflict with each other, and so both processes can contribute to a single spectrum at the same time (Gardner & Done 2015). Our objective is to understand what is the dominant emission mechanism responsible for the soft excess in RX J0439.6−5311.

4.1.1 *Comptonization-dominated models*

In the Comptonization model, the soft excess mainly arise from the Compton up-scattering by electrons with lower temperature and higher opacity than those in the hot corona, which can be modelled with the COMPTT model (Titarchuk 1994). Then the total model in XSPEC is DISKBB+COMPTT+NTHCOMP multiplied by two TBNEW components and a free constant.

Another degree of freedom in this model is the origin of seed photons for the hard X-ray corona, which can be either from the thermal disc emission that can be hot enough to reach the soft X-ray band at small radii (Done et al. 2012), or from the dominant soft excess component, depending on the geometry of the inner disc region that is still not clear. First, we assume the soft X-ray Comptonization occurs in a region between the disc and hot corona, and so seed photons for the hot corona are from the soft excess (hereafter: the CompTT-SE model). This model can fit all three EPIC spectra reasonably well with $\chi^2_\upsilon = 1304/1107$ (Fig. 4a and Table 1). No intrinsic extinction is required by the spectral fitting. The hard X-ray Comptonization shows a very steep spectral shape with the photon index $\Gamma = 2.62^{+0.05}_{-0.06}$. The soft X-ray Comptonization requires an electron temperature of $0.22^{+0.02}_{-0.02}$ keV and an optical depth of $\tau = 16.6^{+8.0}_{-1.8}$, similar to that observed in the soft X-ray excess in all AGN (Gierliński & Done 2004). The temperature of the inner thermal disc is found to be 75^{+11}_{-6} eV, but its normalization is poorly constrained. Removal of this DISKBB component causes little change to the χ^2. Then we assume the hard X-ray Comptonization receives the required seed photons from the inner thermal disc emission (hereafter: the CompTT-Disc model). This model also produces a good fit to the EPIC spectra ($\chi^2_\upsilon = 1305/1107$, Fig. 4b). The best-fitting parameters of the other two components are similar to those in the CompTT-SE model. Therefore, the time-averaged spectra cannot distinguish between these models for the origin of seed photons for the hard X-ray Comptonization component.

4.1.2 *Reflection-dominated models*

In the reflection scenario the soft excess is dominated by an ionized reflection component, and the seed photons for the hot corona come from the inner disc (hereafter: the Reflection-Disc model). We use the RFXCONV model (Ross & Fabian 2005, recoded by Kolehmainen, Done & Díaz Trigo 2011) to calculate the reflection spectrum and then smear it using the KDBLUR model (Laor et al. 1991). The RFXCONV model combines the ionized disc table model from Ross & Fabian (2005) with the Compton reflection model from Magdziarz & Zdziarski (1995).[4] Its parameters include the redshift, the relative reflection normalization (ref_refl $= \Omega/2\pi$) that determines the relative strength between the input spectrum and the reflection spectrum, the iron abundances in the unit of Solar abundances, inclination angle and the ionization parameter ($\log \xi$). A strong constraint of the disc inclination should come from the modelling of iron Kα emission line profile (especially the blue-wing above 6.4 keV), but the S/N of our data is clearly too low to resolve this line profile. Since RX J0439.6−5311 is one of the most highly super-Eddington NLS1s with clean line of sight, a low inclination angle is preferred by the disc wind geometry (Gardner & Done 2015; DJ16; Hagino et al. 2016). Besides, Nandra et al. (1997) studied the iron Kα line profile for a sample of Seyfert 1 galaxies observed by Advanced Satellite for Cosmology and Astrophysics, and found that their inclination angles were clustered at $\sim$30° (also see Fabian et al. 2000). Thus, we fixed the inclination angle of RX J0439.6−5311 at 30°.

This Reflection-Disc model produces as good a fit with a similar χ^2 to the Comptonization models (Fig. 4c and Table 1). The fitting requires the intrinsic corona emission to have an extremely steep slope of $\Gamma = 2.83^{+0.03}_{-0.03}$ with a seed photon temperature of $kT\_bb = 73^{+7}_{-8}$ eV. The smooth soft excess requires highly relativistic smearing with $R_{\rm in} = 2.56^{+0.21}_{-0.19}\ R_{\rm g}$ and an emissivity index of $q = 5.36^{+0.58}_{-0.24}$ in order to suppress all sharp line features in the reflection spectrum. Then the small $R_{\rm in}$ implies a black hole spin of $a \gtrsim 0.86$. The reflecting material is highly ionized ($\log \xi = 3.41^{+0.06}_{-0.05}$) and has a large covering factor of $\Omega/2\pi = 3.70^{+0.38}_{-2.22}$, with $1.38^{+0.08}_{-0.40}\times$ Solar iron abundance. Therefore, the physical scenario can be summarized as that the X-ray corona is very close to the black hole which is fast spinning. The resulting very strong gravitational field would cause a major light bending effect, so that most of the corona emission is illuminating and reflected by the highly ionized inner disc.

However, a simple reflection-dominated model was found to have difficulties in explaining the lack of soft X-ray time lag in PG 1244+026 whose X-ray properties are similar to RX J0439.6−5311 (Alston et al. 2014a). So Kara et al. (2014) proposed

[4] See https://heasarc.gsfc.nasa.gov/xanadu/xspec/manual/node278.html

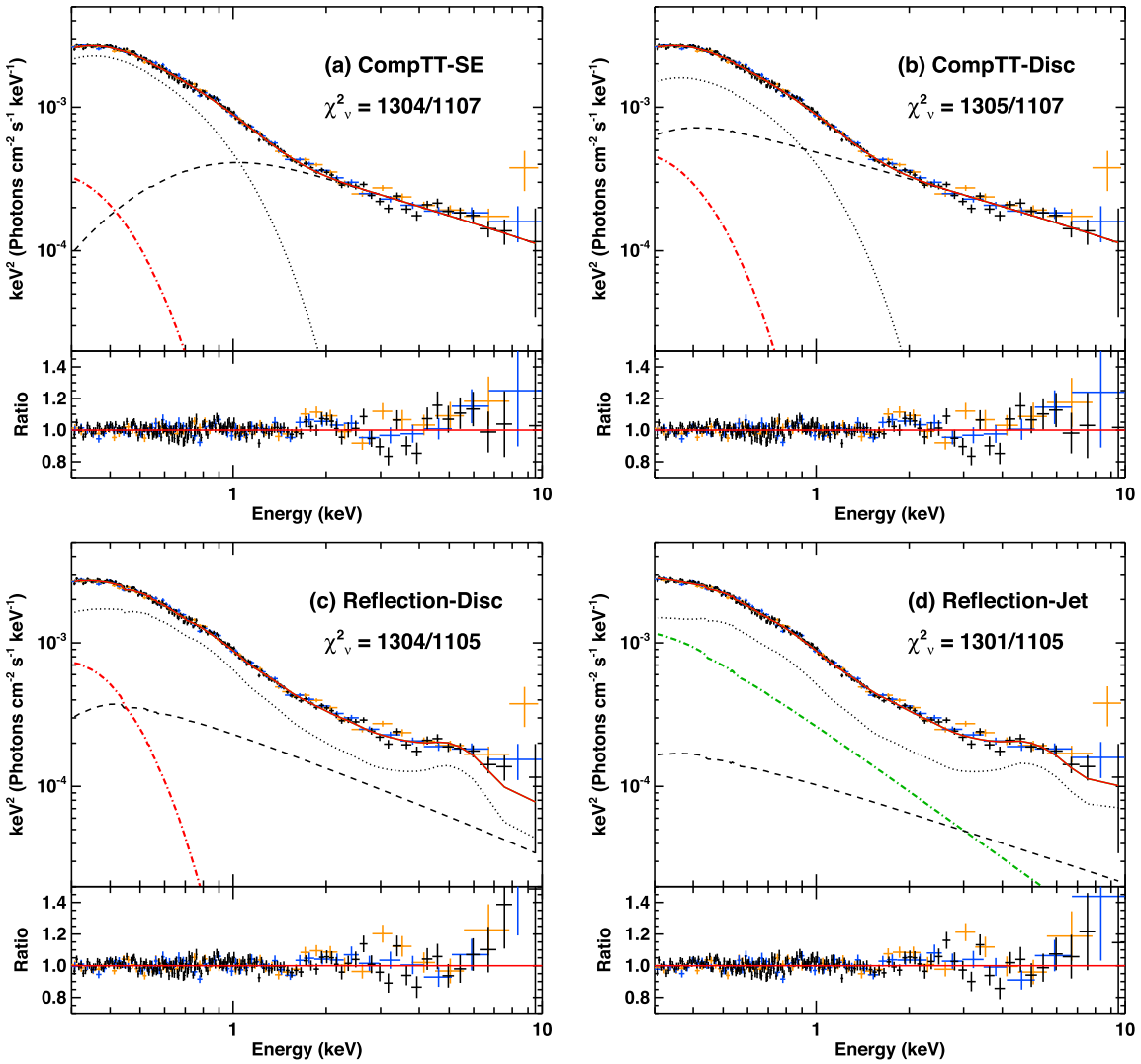

Figure 4. Modelling the time-averaged EPIC spectra, including the EPIC-pn spectrum in black, MOS1 in blue and MOS2 in orange. Panel a: a disc component (DISKBB, red dash–dotted curve), plus a soft X-ray Comptonization component (COMPTT, dotted curve), plus a hard X-ray Comptonization component (NTHCOMP dash curve) whose seed photons are provided by the soft X-ray component. Panel b: the same model components as in panel a, but the seed photons of NTHCOMP come from the inner disc. Panel c: DISKBB (red dash–dotted curve), plus NTHCOMP (dash curve), plus a relativistic reflection component (KDBLUR·RFXCONV, dotted curve). Panel d: similar to panel c, but replacing DISKBB with a power-law jet component (green dash–dotted curve) and replacing NTHCOMP with a simple power-law model. The best-fitting parameters can be found in Table 1.

an additional spectral component associated with the synchrotron emission from a jet to account for part of the soft excess, thereby diluting the time-lag signal in this energy band. However, Gardner & Done (2014) show this is incompatible with the observed soft lead at low frequencies if the fluctuations propagate from the hard X-ray corona close to the black hole, up to the jet, since this gives a soft lag. None the less, a more complex, dual point lamp-post model, Chainakun & Young (2017) is able to produce the lag, so we also apply this jet model to RX J0439.6−5311 (hereafter: the Reflection-Jet model) due to its X-ray spectral similarity to PG 1244+026 (though unlike PG 1244+026 it has no detected radio emission, see Section 7) In Kara et al. (2014), this jet component is modelled with a steep power law to approximate the synchrotron tail in the soft X-ray band. Therefore, we replace the disc component with a steep power law, and also replace the NTHCOMP model with a simple power law in order to be fully consistent with the model adopted in Kara et al. (2014). This model gives $\chi^2_\nu = 1301/1105$, which is equally good as the other models (Fig. 4d). The reflection component is still highly smeared with $R_{\rm in} = 2.44^{+0.14}_{-0.07}\,R_{\rm g}$, but the corona emission has a slightly flatter slope of $\Gamma = 2.70 \pm 0.03$, because the jet component accounts for part of the soft excess.

For comparison, we also ran the spectral fitting for an inclination angle of 60° and put the results in Fig. A1 and Table A1. A higher inclination produces a more bumpy reflection spectrum, which is clearly not favoured by the smoothness of the observed spectra, thus in order to improve the fitting XSPEC will reduce the contribution of reflection component in the smooth soft excess while maintaining the intensity above 4 keV. This explains the maximal black hole spin, smaller hard X-ray power-law photon index, higher iron abundance and smaller reflection fraction as shown by the best-fitting parameters.

4.1.3 *Reflection component in the CompTT-SE model*

Fig. 4(a) shows some positive residuals above 4 keV, implying an extra reflection component in the CompTT-SE model. This reflection

Table 1. Best-fitting parameters in Fig. 4. The upper and lower limits are for the 90 per cent confidence range. In the Reflection-Jet model, POWERLAW1 is for the jet emission and POWERLAW2 is for the intrinsic corona emission. *low* (*up*) indicates the parameter's lower (upper) limit. The disc inclination angle is fixed at 30°.

Model	Component	Parameter	Value
COMPTT	(Fig. 4a)	$\chi^2_\nu = 1304/1107 = 1.18$	
-SE	TBNEW	$N_{\rm H}$ (10^{22} cm^{-2})	$0\ ^{+0.011}_{-0}$
	DISKBB	$T_{\rm in}$ (keV)	$0.075\ ^{+0.011}_{-0.006}$
	DISKBB	Norm	$2.53\ ^{+4.19}_{-2.53} \times 10^3$
	NTHCOMP	Γ	$2.62\ ^{+0.05}_{-0.06}$
	NTHCOMP	$kT_{\rm seed}$ (keV)	Tied to $kT_{\rm e}$
	NTHCOMP	Norm	$4.16\ ^{+0.45}_{-0.46} \times 10^{-4}$
	COMPTT	$kT_{\rm e}$ (keV)	$0.22\ ^{+0.02}_{-0.02}$
	COMPTT	τ	$16.6\ ^{+8.0}_{-1.8}$
	COMPTT	Norm	$0.12\ ^{+0.03}_{-0.07}$
	CONST	(MOS1)	$1.005\ ^{+0.007}_{-0.007}$
	CONST	(MOS2)	$1.009\ ^{+0.008}_{-0.008}$

Model	Component	Parameter	Value
COMPTT	(Fig. 4b)	$\chi^2_\nu = 1305/1107 = 1.18$	
-DISC	TBNEW	$N_{\rm H}$ (10^{22} cm^{-2})	$0\ ^{+0.013}_{-0}$
DISKBB	$T_{\rm in}$ (keV)	$0.075\ ^{+0.004}_{-0.008}$	
	DISKBB	Norm	$3.54\ ^{+3.12}_{-3.54} \times 10^3$
	NTHCOMP	Γ	$2.62\ ^{+0.06}_{-0.07}$
	NTHCOMP	$kT_{\rm seed}$ (keV)	Tied to $kT_{\rm in}$
	NTHCOMP	Norm	$4.90\ ^{+0.32}_{-0.40} \times 10^{-4}$
	COMPTT	$kT_{\rm e}$ (keV)	$0.22\ ^{+0.03}_{-0.03}$
	COMPTT	τ	$17.0\ ^{+19.8}_{-3.0}$
	COMPTT	Norm	$0.082\ ^{+0.03}_{-0.06}$
	CONST	(MOS1)	$1.005\ ^{+0.007}_{-0.007}$
	CONST	(MOS2)	$1.009\ ^{+0.008}_{-0.008}$

Model	Component	Parameter	Value
REFLECTION	(Fig. 4c)	$\chi^2_\nu = 1304/1105 = 1.18$	
-DISC	TBNEW	$N_{\rm H}$ (10^{22} cm^{-2})	$0.017\ ^{+0.010}_{-0.009}$
	DISKBB	$T_{\rm in}$ (keV)	$0.073\ ^{+0.007}_{-0.008}$
	DISKBB	Norm	$9.19\ ^{+6.66}_{-4.04} \times 10^3$
	NTHCOMP	Γ	$2.83\ ^{+0.03}_{-0.03}$
	NTHCOMP	$kT_{\rm seed}$ (keV)	Tied to $kT_{\rm in}$
	NTHCOMP	Norm	$2.41\ ^{+0.50}_{-0.65} \times 10^{-4}$
	KDBLUR	Index	$5.36\ ^{+0.58}_{-0.24}$
	KDBLUR	$R_{\rm in}$ ($R_{\rm g}$)	$2.56\ ^{+0.21}_{-0.19}$
	RFXCONV	rel_refl ($\Omega/2\pi$)[a]	$-3.70\ ^{+2.22}_{-0.38}$
	RFXCONV	$Fe_{\rm abund}$ (Solar)	$1.38\ ^{+0.08}_{-0.40}$
	RFXCONV	log ξ	$3.41\ ^{+0.06}_{-0.05}$
	CONST	(MOS1)	$0.962\ ^{+0.008}_{-0.008}$
	CONST	(MOS2)	$0.966\ ^{+0.008}_{-0.008}$

Model	Component	Parameter	Value
REFLECTION	(Fig. 4d)	$\chi^2_\nu = 1301/1105 = 1.18$	
-JET	TBNEW	$N_{\rm H}$ (10^{22} cm^{-2})	$0.012\ ^{+0.010}_{-0.006}$
	POWERLAW1	Γ	$3.55\ ^{+0.31}_{-0.11}$
	POWERLAW1	Norm	$2.71\ ^{+0.48}_{-0.73} \times 10^{-4}$
	POWERLAW2	Γ	$2.70\ ^{+0.03}_{-0.03}$
	POWERLAW2	Norm	$1.06\ ^{+0.66}_{-0.33} \times 10^{-4}$
	KDBLUR	Index	$5.76\ ^{+0.50}_{-0.36}$
	KDBLUR	$R_{\rm in}$ ($R_{\rm g}$)	$2.44\ ^{+0.14}_{-0.07}$
	RFXCONV	rel_refl ($\Omega/2\pi$)	$-8.52\ ^{+3.25}_{-1.48\,\rm low}$
	RFXCONV	$Fe_{\rm abund}$ (Solar)	$1.00\ ^{+0.11}_{-0.10}$
	RFXCONV	log ξ	$3.12\ ^{+0.08}_{-0.18}$
	CONST	(MOS1)	$0.970\ ^{+0.008}_{-0.007}$
	CONST	(MOS2)	$0.974\ ^{+0.008}_{-0.008}$

Notes. $kT_{\rm seed}$ and $kT_{\rm e}$ are the temperature of the seed photon and electron, separately. τ is the scattering optical depth. 'ref_refl' is the relative reflection normalization in units of $\Omega/2\pi$. [a]A negative 'ref_refl' allows the RFXCONV model to only return the reflection spectrum (see footnote 4). ξ is the ionization parameter defined as the ratio of number density between the ionizing photons and free electrons. DISKBB normalization is defined as $(R_{\rm in}/D_{10})^2 \cos\theta$, where $R_{\rm in}$ is the apparent inner disc radius in km, D_{10} is the source distance in units of 10 kpc, θ is the disc inclination angle. NTHCOMP and POWERLAW normalizations are given in units of photons keV^{-1}cm^{-2}s^{-1} at 1 keV.

can be due to ionized material associated with the inner disc and/or the soft X-ray Comptonization region (Gardner & Done 2014). We attempt to model this by adding an ionized reflection component (RFXCONV) smoothed by the relativistic effects using KDBLUR. A lower limit of 3000 is set for the normalization of the disc component in order to retain its contribution to the soft X-rays. Since the reflection component is weak, not all the parameters can be well constrained, and so we freeze the power-law emissivity index and outer radius of KDBLUR at their default values of 3 and $100R_{\rm g}$. We also fix the Fe abundance at the solar abundance. The inclusion of this reflection component improves the fitting by $\Delta\chi^2 = 11$ for including three additional free parameters (2.5σ significance, Table 2), with the main improvement being the fitting above 4 keV (Fig. 5). The material has low ionization with $\log\xi = 1.34^{+0.25}_{-0.17}$ and a covering factor of $\Omega/2\pi = 1.17^{+0.54}_{-0.54}$. The other parameters are similar to those found in the previous CompTT-SE fitting, including a large photon index of $\Gamma = 2.72^{+0.05}_{-0.07}$. We also find the best-fitting $R_{\rm in} = 2.80^{+2.74}_{-1.80}\ R_{\rm g}$, corresponding to a spin parameter of $a = 0.82^{+0.18}_{-0.68}$ that is poorly constrained. However, if we allow the Fe abundance to be a free parameter, the best-fitting parameters would be $Fe_{\rm abund} = 3.7$, $R_{\rm in} = 4.35\,R_{\rm g}$ and $\Gamma = 2.74$ with an improved $\Delta\chi^2 = 6$ for one additional free parameter (2.4σ significance), the rest parameters are little changed. Furthermore, if we assume that the reflecting material is mainly associated with the soft X-ray component, which is several tens to hundreds of $R_{\rm g}$ away from the hot corona as suggested by the time-lag analysis (see Section 6), then we can place a lower limit of $10R_{\rm g}$ for $R_{\rm in}$. Then we find $R_{\rm in}$ reaches its lower limit of $10R_{\rm g}$ and a worse fit by $\Delta\chi^2 = 2$ compared to the original value, and the other parameters are all similar to those found previously, except that the covering factor decreases slightly to $\Omega/2\pi = 0.80$.

The above results from the spectral fitting can be understood as follows. First, the excess flux above 4 keV requires a reflection component, while the soft excess is so smooth that it does not favour

Table 2. Best-fitting parameters in Fig. 5. The inclination angle is fixed at 30°. 'low' indicates that the parameter reaches its lower limit during the fitting. Units of the normalizations are the same as given in Table 1.

Model	Component	Parameter	Value
COMPTT-SE	(Fig. 5)	$\chi^2_\nu = 1293/1104 = 1.17$	
	TBNEW	$N_{\rm H}$ (10^{22} cm^{-2})	$0.007\ ^{+0.024}_{-0.007}$
(+RFXCONV)	DISKBB	$T_{\rm in}$ (keV)	$0.075\ ^{+0.007}_{-0.005}$
	DISKBB	Norm	$3.00\ ^{+8.85}_{-0\,\rm low} \times 10^3$
	NTHCOMP	Γ	$2.72\ ^{+0.05}_{-0.07}$
	NTHCOMP	$kT_{\rm seed}$ (keV)	Tied to $kT_{\rm e}$
	NTHCOMP	Norm	$4.21\ ^{+0.32}_{-0.38} \times 10^{-4}$
	COMPTT	$kT_{\rm e}$ (keV)	$0.22\ ^{+0.01}_{-0.01}$
	COMPTT	τ	$16.5\ ^{+7.2}_{-1.6}$
	COMPTT	Norm	$0.12\ ^{+0.04}_{-0.07}$
	KDBLUR	Index	3.0 fixed
	KDBLUR	$R_{\rm in}$ ($R_{\rm g}$)	$2.80\ ^{+2.74}_{-1.80\,\rm low}$
	RFXCONV	rel_refl ($\Omega/2\pi$)	$-1.17\ ^{+0.54}_{-0.54}$
	RFXCONV	$Fe_{\rm abund}$ (Solar)	1.0 fixed
	RFXCONV	log ξ	$1.34\ ^{+0.25}_{-0.17}$
	CONST	(MOS1)	$1.002\ ^{+0.008}_{-0.007}$
	CONST	(MOS2)	$1.006\ ^{+0.008}_{-0.008}$

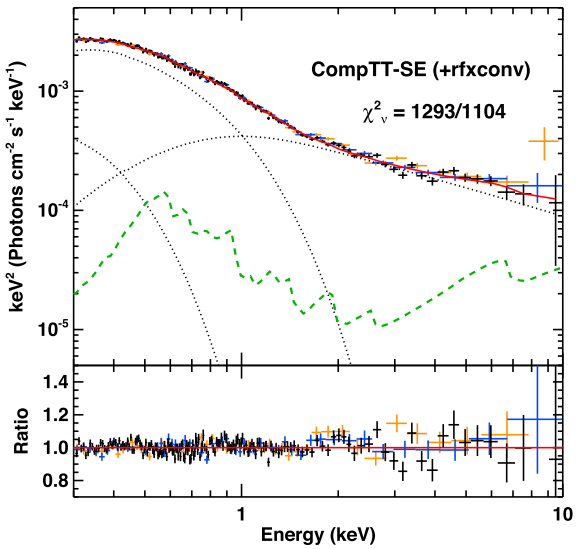

Figure 5. Adding a reflection component to the CompTT-SE model in Fig. 4(a). The dash green curve shows the ionized reflection component. The best-fitting parameters are in Table 2.

any sharp line features,[5] and so a small $R_{\rm in}$ is required to smear all the line features in the reflection spectrum. A low ionization state is also favoured in order to further reduce the intensity of these lines. When we allow the Fe abundance to be a free parameter, the fitting increases the abundance to account for the excess flux above 4 keV, and also reduces the strength of the reflection component in the soft excess, and so a small $R_{\rm in}$ is no longer required. When a lower limit of $10R_{\rm g}$ is set for $R_{\rm in}$, the line features in the reflection spectrum are more sharp, and so the fitting reduces the flux of the reflection component by reducing its covering factor, accompanied by a worse χ^2. Therefore, we conclude that the small $R_{\rm in}$ is mainly due to the contradiction between the sharp line features in the reflection spectrum and the observed smooth soft excess, rather than due to a broad iron Kα feature.

[5] The smoothness of the soft excess is also confirmed by the two RGS spectra, where we found no significant sharp emission/absorption lines, which also rules out any significant warm absorbers along the line of sight.

5 COMBINED SPECTRAL AND VARIABILITY ANALYSIS

5.1 Frequency-dependent rms and covariance spectra

Previous spectral analysis has suggested that the time-averaged spectra are highly degenerate to different spectral models, and so we need to use information on variability in order to break the spectral degeneracy and so distinguish between these models. Compared to the rms spectra that show the total intrinsic variability in every energy bin, a covariance spectrum shows all spectral components that vary coherently with a chosen energy band (i.e. the reference band). Therefore, it would have an identical shape (but with smaller error bars) as the rms spectrum if there is only one variability pattern over the entire energy band. This technique was first introduced by Wilkinson & Uttley (2009) to increase the S/N of the rms spectrum (also see the review by Uttley et al. 2014), and then was adopted by Middleton, Uttley & Done (2011) to disentangle the soft excess from the hard X-ray power law in RE J1034+396. J13 further explored the capability of this technique by producing the frequency/reference-band-dependent covariance spectra, which showed that the soft excess in PG 1244+026 strongly favoured the Comptonization origin rather than reflection. RX J0439.6−5311 is similar to PG 1244+026 in terms of their X-ray spectra. It is important to understand if their X-ray variabilities are also similar. We apply various spectral-timing techniques to explore the variability properties of RX J0439.6−5311 in both energy and frequency domains.

First, we multiply the fractional rms to the time-averaged spectrum of EPIC-pn to derive the absolute rms spectra. For the covariance spectra, we choose 0.3–1 keV as the soft X-ray reference band (hereafter: SX) and 2–10 keV as the hard X-ray reference band (hereafter: HX). The frequency band is divided into the LF band and HF band, the same as for the rms spectra. So in total there are four covariance spectra, which can be identified as HF-HX, HF-SX, LF-HX and LF-SX. To produce covariance spectra, a band-limited light curve is derived by applying a frequency filter in the Fourier domain. Then the prescription in Uttley et al. (2014) is used to calculate their fractional covariances in every energy bin relative to the reference band. Note that energy bins inside the reference band are excluded from the reference band before calculating the covariance. Finally, we multiply the fractional covariances to the time-averaged spectra of the EPIC-pn to derive the covariance spectra (see J13 for further details). This procedure is repeated for different frequency and reference bands to produce all four versions of covariance spectra.

Fig. 6 shows the comparison between the time-averaged spectrum and the rms and covariance spectra in both LF and HF bands. In order to compare the strength of the soft excess, we use the NTHCOMP model component in the best-fitting CompTT-SE model in Fig. 4(a) to fit the variability spectra within the 2–10 keV band with a fixed photon index, and then extrapolate the model down to lower energies to show the soft excess ('Ratio' panels in Fig. 6). In the HF band (Fig. 6a), we can see that the normalizations of the HF-SX and HF-HX covariance spectra are both lower than the HF rms spectra,

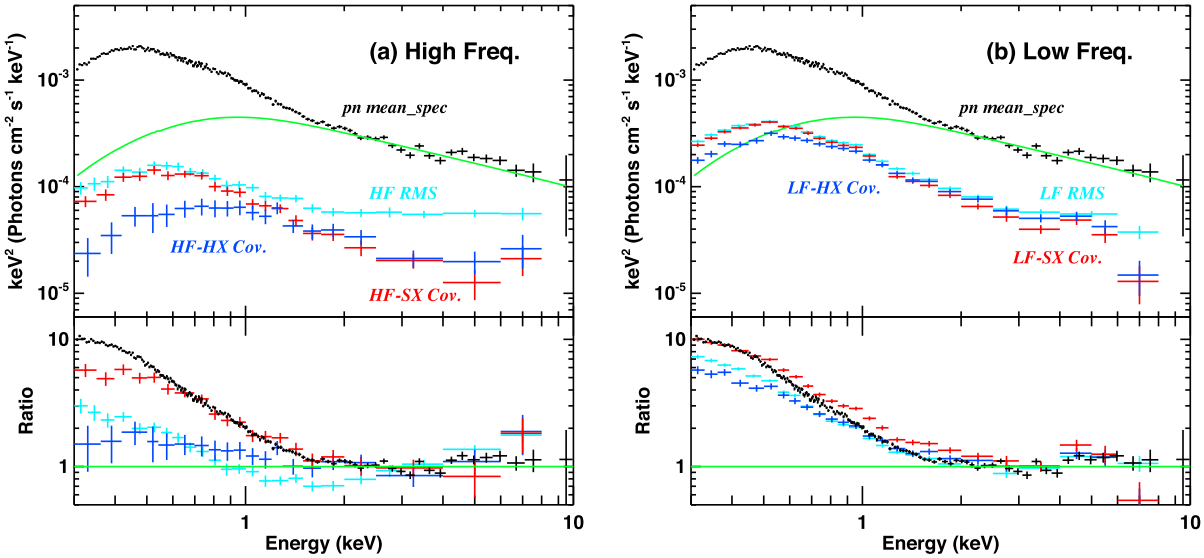

Figure 6. A direct comparison between the time-averaged spectrum, rms and covariance spectra from EPIC-pn for the high-frequency band (Panel a) and the low-frequency band (Panel b). In each panel, the green solid line shows the hard X-ray Comptonization component in the CompTT-SE model in Fig. 4(a). 'Ratio' panels show the strength of the soft excess in every spectrum relative to the extrapolation of the best-fitting Comptonization model within the 2–10 keV band, assuming the same photon index as in the time-averaged spectrum.

which should be due to the Poisson noise contamination to the HF covariance. However, we also find different shapes among these spectra. For example, the HF rms spectrum is clearly flatter than the time-averaged spectra and covariance spectra above 2 keV, which implies some uncorrelated variability in the hard X-rays. The HF-SX covariance spectrum has a similar shape to the time-averaged spectra except below 0.6 keV, indicating the presence of an extra component with no HF variability, e.g. an inner disc component. The HF-HX covariance spectrum has the weakest soft excess compared to the other spectra in Fig. 6(a), indicating that only a small fraction of the HF variability in the hard X-ray component is correlated with the soft X-ray components. Similar results can be found in the LF band (Fig. 6b) where the LF covariance is less affected by the Poisson fluctuation. But the LF rms spectrum shows a similar steep spectral slope as the other spectra above 2 keV, indicating no extra uncorrelated LF variability in the hard X-rays. Since the differences among these variability spectra are quite distinct, we can use them to test different models and so break the spectral degeneracy.

5.2 Modelling the covariance spectra

In the two Comptonization-dominated models, each of them contains two Comptonization components, plus a disc component and a weak reflection component. We assume the disc component does not vary within the 120 ks observing time, so it does not contribute to the covariance spectra. The reflection component is not well constrained as it is overwhelmed by the other components across the entire 0.3–10 keV band, so we ignore its contribution in the covariance spectra unless the other major components are not sufficient. The two Comptonization components can both vary but with different timing properties (as implied by the PSD and rms spectra), and so they should have different contributions in different types of covariance spectra. Therefore, we assume that their spectral shapes do not change in the covariance spectra, but their normalizations are free to change.

First, we apply the CompTT-SE model to the EPIC-pn time-averaged spectrum and all four covariance spectra, simultaneously. Fig. 7 shows that the CompTT-SE model can produce a good fit to all spectra with a total $\chi^2_v = 842/721$. The key parameters are all consistent with those found previously from fitting the time-averaged spectra alone (see Table 3). The HF-HX covariance spectrum is totally dominated by the hard X-ray Comptonization component, but there is also a small contribution from the soft excess component, indicating the presence of some reprocessed hard X-ray emission in the soft X-ray region, which is also consistent with the presence of a weak reflection component in Fig. 5. The LF covariance spectra consist of significant contributions from both soft and hard X-ray Comptonization components, indicating a strong LF coherence between these two components (also see Section 6). Moreover, all covariance spectra are well fitted below ∼0.5 keV, confirming that the non-variable accretion disc component only contributes to the soft excess on longer time-scales.

Then we apply the CompTT-Disc model to all the spectra. In this case the hard X-ray Comptonization component appears too flat compared to the curvature of the HF-HX covariance spectrum in the soft X-ray band (Fig. 8). Below ∼1.5 keV we find $\chi^2_v = 20/12$ for the HF-HX covariance spectrum, which is clearly much worse compared to $\chi^2_v = 10/12$ in the case of the CompTT-SE model. This suggests that the temperature of the seed photons from the inner disc is too low. The same result was found in PG 1244+026 (J13), implying that this is probably a common property among similar NLS1s with high mass accretion rates.

In the two reflection-dominated models, the spectrum mainly consists of an underlying Comptonization component from the hot corona which is the primary varying component, and an ionized reflection component. The variability of the reflection component also comes from the hot corona, with some smearing and time lag. In the Reflection-Disc model, the disc is not varying on these short time-scales, so only the corona and reflection components contribute to the covariance spectra. Fig. 9(a) shows that this model can roughly match the HF-FX covariance spectrum in the soft X-ray band, with $\chi^2_v = 16/12$ below 1.5 keV.

In the Reflection-Jet model, the jet component can also vary on various time-scales, and may be partly correlated with the corona

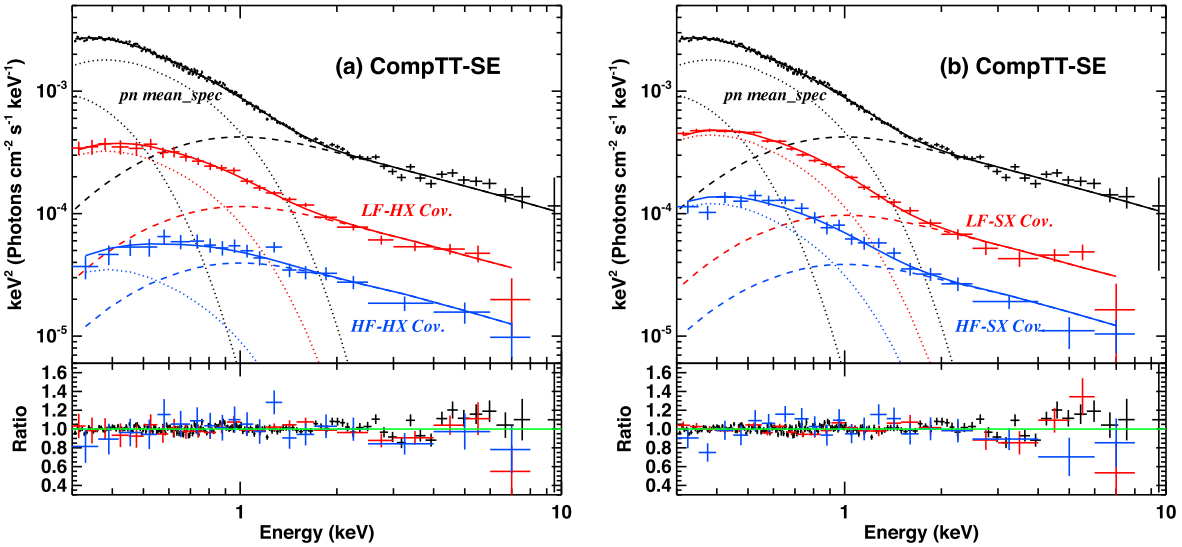

Figure 7. Applying the CompTT-SE model to the EPIC-pn time-averaged spectrum (black) and all four types of covariance spectra. For clarity we plot the spectra in two panels. Panel a shows the HF-HX (blue) and LF-HX (red) covariance spectra. Panel b shows the HF-SX (blue) and LF-SX (red) covariance spectra. It is clear that the CompTT-SE model can produce good fits to all the spectra (see Section 5.1).

Table 3. The best-fitting parameters of the CompTT-SE model to the time-averaged spectrum and all four covariance spectra from EPIC-pn in Fig. 7. The upper and lower limits give the 90 per cent confidence range. Units of the normalizations are the same as given in Table 1.

Model	Component	Parameter	Value
COMPTT-SE	(Fig. 7)	$\chi^2_\nu = 842/721 = 1.17$	
mean-spec	TBNEW	$N_{\rm H}$ (10^{22} cm^{-2})	$0\ ^{+0.034}_{-0}$
	DISKBB	$T_{\rm in}$ (keV)	$0.080\ ^{+0.004}_{-0.004}$
	DISKBB	Norm	$5.41\ ^{+1.79}_{-1.26} \times 10^3$
	NTHCOMP	Γ	$2.67\ ^{+0.06}_{-0.06}$
	NTHCOMP	$kT_{\rm seed}$ (keV)	Tied to $kT_{\rm e}$
	NTHCOMP	Norm	$4.28\ ^{+0.36}_{-0.37} \times 10^{-4}$
	COMPTT	$kT_{\rm e}$ (keV)	$0.21\ ^{+0.01}_{-0.01}$
	COMPTT	τ	$18.6\ ^{+1.43}_{-1.29}$
	COMPTT	Norm	$9.12\ ^{+1.3}_{-1.1} \times 10^{-2}$
cov-LF-HX	NTHCOMP	Norm	$1.16\ ^{+0.10}_{-0.10} \times 10^{-4}$
	COMPTT	Norm	$1.65\ ^{+0.20}_{-0.17} \times 10^{-2}$
cov-HF-HX	NTHCOMP	Norm	$4.01\ ^{+0.40}_{-0.39} \times 10^{-5}$
	COMPTT	Norm	$1.78\ ^{+0.41}_{-0.41} \times 10^{-3}$
cov-LF-SX	NTHCOMP	Norm	$9.84\ ^{+1.05}_{-1.04} \times 10^{-5}$
	COMPTT	Norm	$2.23\ ^{+0.23}_{-0.20} \times 10^{-2}$
cov-HF-SX	NTHCOMP	Norm	$3.90\ ^{+0.46}_{-0.45} \times 10^{-5}$
	COMPTT	Norm	$6.16\ ^{+0.77}_{-0.67} \times 10^{-3}$

component because the corona may be considered as being the base of the jet (Kara et al. 2014). So we allow the jet, corona and reflection components all to contribute to the covariance spectra. We also find this model cannot fit the HF-HX covariance spectrum, with $\chi^2_\nu = 40/13$ for the energy band below 1.5 keV (Fig. 9b). Therefore, we conclude that the CompTT-Disc model and reflection-dominated models cannot reproduce all covariance spectra, especially the HF-HX covariance spectrum where a clear soft X-ray roll-over is seen, while the two Comptonization components in the CompTT-SE model can produce a good fit to all four covariance spectra, simultaneously.

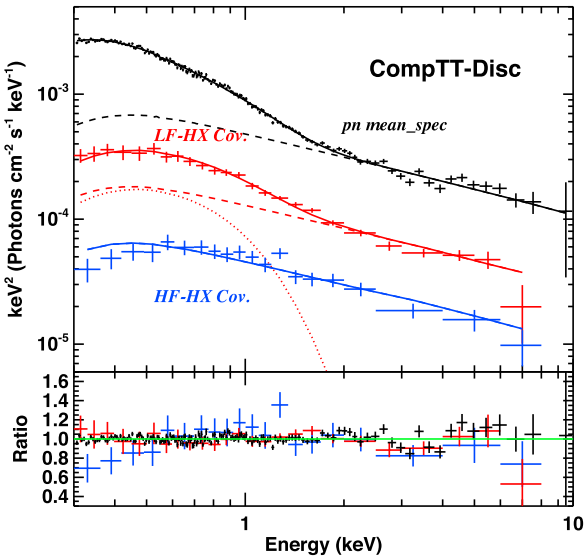

Figure 8. Similar to Fig. 7, but applying the CompTT-Disc model. The HF-HX covariance spectrum is not as well fitted below 1 keV.

5.3 Modelling the rms spectra

Although among the four models the CompTT-SE model is the best one that can reproduce the time-averaged and all covariance spectra, we identify a problem when applying it to the rms spectra. The hard X-ray slope measured from the time-averaged spectrum is steeper than the HF rms spectra, so the CompTT-SE model underpredicts the HF rms above ∼2 keV (see the cyan dash line in Fig. 10a). However, we do not see any similar excess variability in the LF band in either the LF rms spectrum or the covariance spectra (Fig. 6b), and so this is an independent variable component in the HF band only.

However, we note that there could also be an ionized reflection component in the CompTT-SE model as shown in Fig. 5, and this component can also vary in the HF. Thus, we add this component to fit all three time-averaged EPIC spectra and the two rms spectra simultaneously. This reflection component does improve

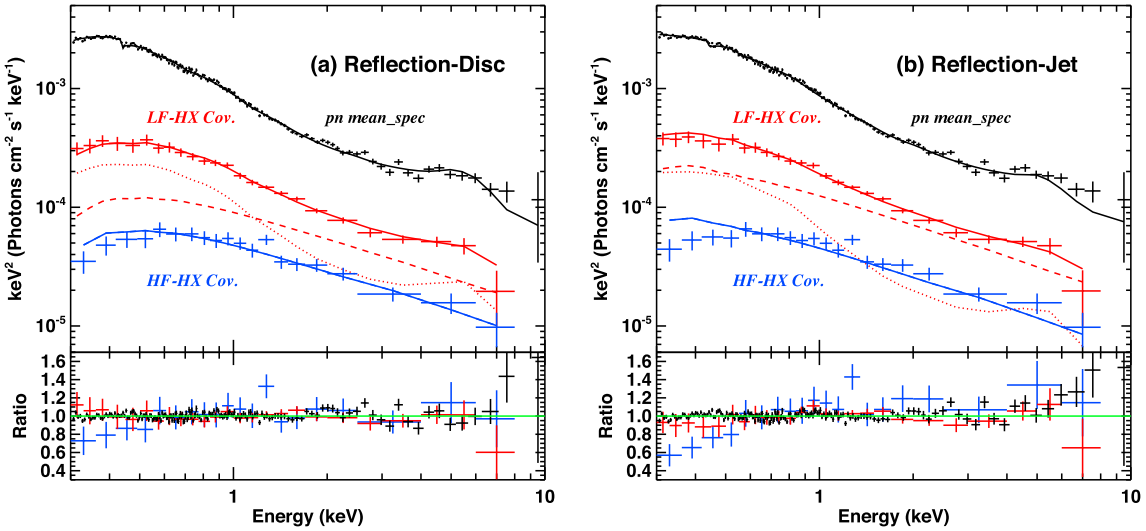

Figure 9. Applying the reflection-dominated models to the EPIC-pn time-averaged spectrum (black), HF-HX covariance spectrum (blue) and LF-HX covariance spectrum (red). Panel a shows the results for the Reflection-Disc model. Panel b shows the results for the Reflection-Jet model. Both models have some difficulties in fitting the HF-HX covariance spectrum below ∼1 keV.

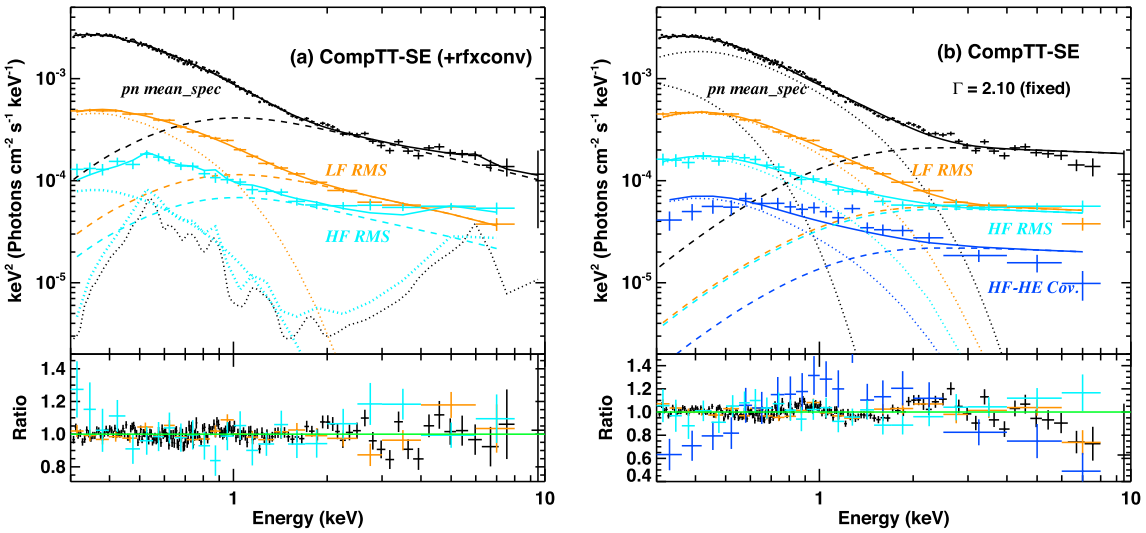

Figure 10. Fitting the EPIC time-averaged spectra, LF and HF rms spectra with the CompTT-SE model. Panel a shows the fitting with the CompTT-SE plus reflection model in Fig. 5(b) (but with no lower limit for $R_{\rm in}$), assuming the reflection component can contribute extra variability. For clarity we only plot the time-averaged spectrum from EPIC-pn and the two rms spectra. Panel b shows the CompTT-SE model fitting with the hard X-ray photon index fixed at 2.1. We also plot the HF-HX covariance spectrum that cannot be well fitted in this case.

the fitting to the HF rms spectrum above 4 keV. The best-fitting $\chi^2_\nu = 1361/1151$, which shows an improvement of $\Delta\chi^2 = 46$ for three extra free parameters (6.2σ significance). In this fitting, $R_{\rm in}$ also reaches its lower limit of 10 $R_{\rm g}$. If we do not put a lower limit for $R_{\rm in}$, then the best-fitting value would be $5.13^{+1.40}_{-1.63}$ $R_{\rm g}$ and χ^2 improves by 10 for 1 extra free parameter (3.2σ significance, Fig. 10a). The lack of HF covariance between this reflection component and the primary hard X-ray corona component can be explained as due to the smearing of signal during the reverberation process. However, in this scenario we would expect that compared to the hard X-ray corona component, the relative contribution of the reflection component to the time-averaged spectrum should be more than to the HF rms spectrum, which is opposite to the fitting seen in Fig. 10(a). Moreover, there is still a flux discrepancy within the 2–4 keV band, and the HF rms spectrum appears smoother than the reflection component below 1 keV. Therefore, we cannot conclude that the reflection component is responsible for the excess HF variability above 4 keV.

Another possibility is that the hard X-ray Comptonization component is indeed flatter. To test this we fix the photon index Γ at 2.1 and rerun the fitting. The new fitting has $\chi^2_\nu = 1484/1153$ (Fig. 10b), which is significantly worse than it was when Γ was a free parameter ($\Delta\chi^2 = 83$ for one less degree of freedom). With such a flatter hard X-ray component, the fitting requires the soft X-ray Comptonization component to extend further into the hard X-rays with $kT_{\rm e} = 0.39^{+0.04}_{-0.03}$ keV and $\tau = 10.6^{+0.7}_{-0.8}$. Since the soft X-ray Comptonization region probably extends over several tens of $R_{\rm g}$ (see Section 6), the electrons in it may have a wider temperature distribution than a single value, so it is indeed possible for the soft X-ray component to be more extended than a single COMPTT model. However, If we add all four types of covariance spectra to the fitting, the best fit has $\chi^2_\nu = 1642/1236$, which is much worse than

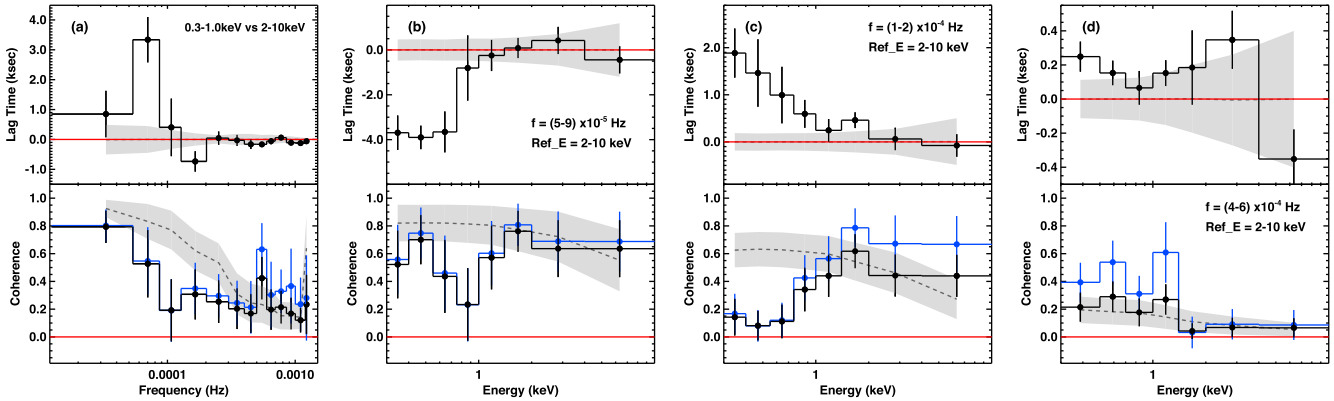

Figure 11. Energy- and frequency-dependent time lag and coherence. A negative time lag indicates the soft X-ray emission lags the hard X-ray. In the coherence panel, the blue points are the coherences after Poisson noise correction (Vaughan & Nowak 1997). In every panel, the dash curve and shaded region are the mean and $\pm1\sigma$ dispersion from our simulations assuming an intrinsically full-correlated zero-lag interband correlation (see Section 6). The reference band for the time lag is 2–10 keV, and the simulation is based on the PSD of 2–10 keV. Results using different reference bands and PSDs can be found in Figs B1–B3.

the free Γ case. We notice that this model also has difficulties in fitting the HF-HE covariance spectrum (Fig. 10b, blue spectrum). Therefore, this flatter hard X-ray Comptonization model is not a plausible solution. More observations especially above 4 keV could provide better constraints on the shape of the hard X-ray component and help to identify the origin of this hard X-ray excess variance.

6 TIME-LAG ANALYSIS

6.1 Lag and coherence spectra

The strongly correlated X-ray variability seen in RX J0439.6−5311 also allows us to measure the time lags between different energy bands in different frequency ranges. These time lags can provide crucial information about the absolute distances between distinct physical regions. The rms and covariance spectra have shown that the HF variability seen in RX J0439.6−5311 is mainly associated with the hard X-rays, while more LF variability is found in the soft X-rays. Simply associating these variability time-scales with the dynamic time-scale of the accretion flow at different radii, they suggest the soft X-ray Comptonization region should be more extended than the compact hot corona region. Then the time lag between the soft and hard X-rays can indicate the distance between these two physical regions. Note that due to the small contribution of the hard X-ray component in the soft X-ray band, the observed time lag is only a diluted measurement of the intrinsic time lag between the two spectral components (e.g. Uttley et al. 2014).

We follow the prescription in Vaughan & Nowak (1997) and Nowak et al. (1999) (also see Vaughan et al. 2003b; Arévalo et al. 2008 for detailed descriptions) to calculate the cross-spectrum between light curves (400 s binned) of two energy bins. Since the strong LF variability can easily introduce a bias via the red noise leak (e.g. Vaughan, Fabian & Nandra 2003a), we use the whole light curve to do the Fourier transform instead of dividing it into some segments. The cross-spectrum is binned in frequency with a geometrical step of 1.4. Then the coherence and time lag can be derived from the cross-spectra in different frequency bins (Bendat & Piersol 1986). Poisson noise correction is applied to the coherence using the algorithm in Vaughan & Nowak (1997). The standard conventions are followed, so that a positive time lag indicates the soft X-rays lead the hard X-rays. A zero coherence indicates no correlated variability, while a coherence of unity indicates a fully correlated variability.

However, the Vaughan & Nowak (1997) analytic prescription for the effect of the error bars is only valid in the regime where the intrinsic power is higher than the Poisson noise. This is not true at high energies, so we also perform Monte Carlo simulations to better estimate the effect of errors on the coherence and time-lag spectra (Alston et al. 2014b). First, we use the 2–10 keV PSD and the method of Timmer & Koenig (1995) to simulate new light curve realizations of the same length and binning and intrinsic power spectra. We then add errors based on the observed measurement errors for each energy band. In this way, we obtain light curves in different energy bins with fully correlated intrinsic variability like that seen in 2–10 keV with zero lag. Then we use the same method to calculate coherence and lag spectra between these simulated light curves. We repeat this simulation for 10 000 times to measure the random fluctuation of the coherence and lag spectra (Fig. 11).

We notice that the result of simulation much also depend on the input PSD. Fig. 2 has shown that the 2–10 keV PSD contains much more HF variability than the 0.3–1 keV PSD (similar to the 0.3–10 keV PSD as most of the X-ray counts come from the 0.3–1 keV band). This means that the same Poisson errors will have bigger impact on the light curves simulated from the 0.3–1 keV PSD than the 2–10 keV. Thus, we also run the same simulations for the 0.3–1 keV PSD and use them as comparison (Figs B1–B3).

Fig. 11(a) upper panel shows the lag versus frequency between 0.3–1 keV (SX) and 2–10 keV (HX). The shape of this lag-frequency spectrum is commonly observed in many other AGN (De Marco et al. 2013; Kara et al. 2016), with a hard X-ray lag in the LF band and a weak soft X-ray lag in the HF band. The shaded regions indicate the $\pm1\sigma$ fluctuation of these spectra caused by Poisson errors as determined from the Monte Carlo simulations. Fig. 11(a) lower panel shows that the observed coherence-frequency spectrum is slightly lower than the simulation based on the 2–10 keV PSD, but is more consistent with the simulation based on the 0.3–1 keV PSD (Fig. B1a). This means that the additional power at high frequencies in the 2–10 keV PSD introduces an intrinsic decoherence especially above 5×10^{-4} Hz.

While the error bars clearly have a large impact on the data, we do observe one significant positive lag of 3.4 ± 0.8 ks within (5–9) $\times 10^{-5}$ Hz with high coherence, and an enhanced coherence

within (4–6) × 10^{-4} Hz with a weak negative lag. There is also a negative lag within (1–2) × 10^{-4} Hz with marginal significance. Therefore, we select these bands to calculate the lag/coherence spectra relative to the 2–10 keV band. Fig. 11(b–d) shows the results (equivalent results relative to the 0.3–1 keV band can be found in Figs B2 and B3).

For the (5–9) × 10^{-5} Hz band (Figs 11b and B2b), there is a high coherence in the soft X-ray band with no time lag (lower panel), indicating that a single component dominates the soft excess, consistent with the spectral decomposition of the CompTT-SE model. Compared to the fully correlated zero-lag simulation (shaded region), the coherence seems to drop below 0.5 keV (although with large error bars), which is likely due to the dilution of the non-variable disc component. Furthermore, the coherence also seems to be lower than the simulation within 0.8–2 keV, indicating that there might be a transition of the dominated spectral component within this energy range, i.e. consistent with the transition between the soft and hard X-ray Comptonization components. The most noticeable feature is the increasing time lag from the soft to hard X-rays (Fig. 11b upper panel). The time lag below 1 keV is ~ -4 ks with a moderate coherence of $\sim$0.6, and it is more than 4σ away from the random fluctuation of the zero-lag simulation. In the (1–2) × 10^{-4} Hz and (4–6) × 10^{-4} Hz bands (Fig. 11c, d), there appears to be a 0.3–1 keV lag of $\sim$2 ks and 200 s, separately. But the corresponding coherences in these energy bands are $\lesssim$0.2, and so we do not consider them as robust time-lag detections. However, it is worth noting that a small soft X-ray lag was found in the HF band in PG 1244+026 with higher S/N (Alston et al. 2014a).

6.2 Modelling the LF lag spectrum

Comptonization and reflection dominated models have different predictions on the time lag. In the Comptonization-dominated models, a fluctuation propagates from the soft X-ray region to the hard, thereby introducing a hard X-ray time lag. In the reflection-dominated model, the reflection component lags behind the primary corona component, thereby producing a time lag around the broad Kα band and a soft X-ray lag. However, the mixed contributions from different components in every energy bin can easily dilute the time-lag signal between different energy bands. Therefore, we also perform a light-curve simulation to show the predicted time lags in every model and compare them to the LF lag spectrum.

We simulate light curves from the 2 to 10 keV PSD in the same way as in the previous section. Similar to previous studies (e.g. Alston et al. 2014a; Kara et al. 2014), we assume identical light curves for every spectral component, but shift them by an assumed time lag, and then combine them in every energy bin according to the fractional contribution of each component as derived from the fitting of the time-averaged spectra in Fig. 4. This method does not take into account of any intrinsic difference in the PSD of the various spectral components, but it can still reveal the effect of multicomponent contributions within the lag spectrum. We examined various time-lag assumptions between different spectral components in all models, in order to obtain the best match to the observed LF lag spectrum. The time-lag assumptions are listed in Table 4. Note that 5000 s is approaching the upper limit for the detectable time lag in the (5–9) × 10^{-5} Hz frequency band. For every model, the simulation was repeated for 10 000 times to derive the mean lag spectrum.

Fig. 12 shows that it is difficult for the reflection-dominated models to reproduce the LF lag spectrum with the reverberation lag (also see Fig. B1d for the equivalent result relative to the 0.3–1 keV band). This is mainly because the reflection component has strong contributions across the entire 0.3–10 keV band, especially dominating the 0.3–1 keV band, and so the time lag relative to the 2–10 keV band is heavily diluted, and can only produce small lag signals around zero. We also tried fixing the hard X-ray Γ at 2.3 in order to produce a more similar spectral decomposition to that obtained for PG 1244+026 in Kara et al. (2014) (Fig. 13, Table 5). For this new fit, we also tried to add a weak disc component to the soft excess similar to the CompTT-SE model, but its normalization was found to be consistent with zero within less than 2σ, so we no longer consider any disc emission in it. This new fit is considerably worse than the free Γ case by $\Delta\chi^2 = 46$ for one less free parameter. But this spectral decomposition can produce a negative lag at soft X-rays (green dash curve in Fig. 12), because now the 0.3–1 keV is dominated by the jet component instead of the reflection component. However, even the assumption of 5 ks time lag can only produce ~ -1 ks lag in the soft X-ray band, and so this model still fails to reproduce the observed LF lag spectrum.

On the other hand, it is much easier for the Comptonization-dominated models to reproduce the LF lag spectrum with the propagation lag. Fig. 12 shows that both CompTT-Disc model and CompTT-SE model can reproduce the broad lag profile below 1 keV, but CompTT-Disc model slightly underpredicts the time lag below 1 keV because the hard X-ray component extends into the

Table 4. The assumed time lags in every model simulation in Fig. 12. In each model, the time lags are relative to the disc or jet component.

CompTT-SE	Disc	Hard X-ray corona	Soft X-ray Compton
	0 s	300 s	5000 s
CompTT-Disc	Disc	Hard X-ray corona	Soft X-ray Compton
	0 s	300 s	5000 s
Reflection-Disc	Disc	Hard X-ray corona	Reflection
	0 s	300 s	5000 s
Reflection-Jet	Jet	Hard X-ray corona	Reflection
	0 s	300 s	5000 s

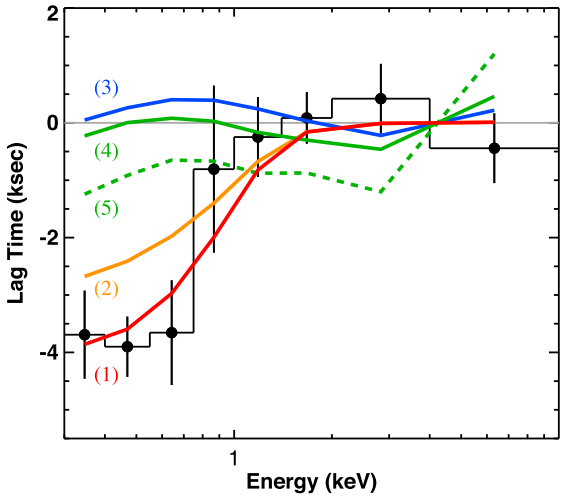

Figure 12. Comparison between the LF lag spectrum (the same as Fig. 11b) and the time-lag predictions of various models. Curves are simulated from the spectral decompositions in Fig. 4 with (1) CompTT-SE model, (2) CompTT-Disc model, (3) Reflection-Disc model and (4) Reflection-Jet model, respectively. The CompTT-SE model shows the best match to the lag spectrum. The green dash curve (5) is also based on the Reflection-Jet model but with the new fitting in Fig. 13.

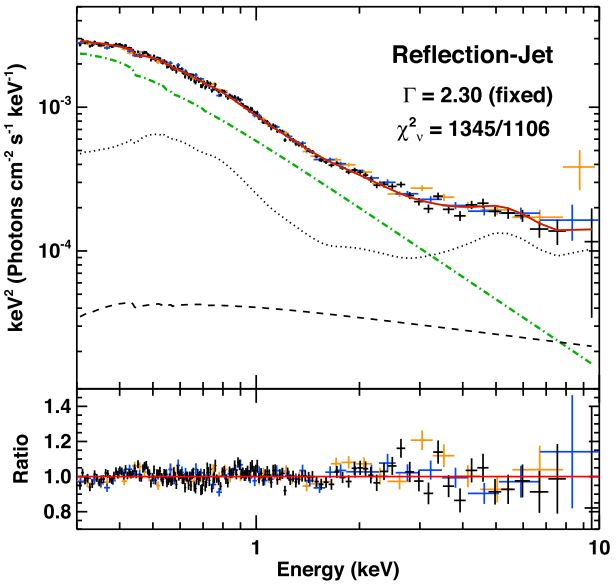

Figure 13. Refitting the time-averaged spectrum with the Reflection-Jet model, but with the hard X-ray Γ fixed at 2.3 in order to reduce the contribution of the reflection component in the soft excess. Spectral components are the same as those in Fig. 4(d). The best-fitting parameters are listed in Table 5.

Table 5. Best-fitting parameters in Fig. 13. 'low' indicates the parameter reaches its lower limit separately during the fitting. POWERLAW normalization is given in units of photons $\mathrm{keV^{-1}cm^{-2}s^{-1}}$ at 1 keV.

Model	Component	Parameter	Value
REFLECTION	(Fig. 13)	$\chi^2_\nu = 1345/1106 = 1.22$	
-JET	TBNEW	$N_{\rm H}$ (10^{22} cm^{-2})	$0.023\ ^{+0.008}_{-0.008}$
	POWERLAW1	Γ	$3.61\ ^{+0.08}_{-0.07}$
	POWERLAW1	Norm	$6.13\ ^{+0.27}_{-0.24} \times 10^{-4}$
	POWERLAW2	Γ	2.30 fixed
	POWERLAW2	Norm	$4.27\ ^{+0.58}_{-0.38} \times 10^{-5}$
	KDBLUR	Index	$5.76\ ^{+0.56}_{-0.53}$
	KDBLUR	$R_{\rm in}$ ($R_{\rm g}$)	$2.69\ ^{+0.16}_{-0.13}$
	RFXCONV	rel_refl ($\Omega/2\pi$)	$-10.0\ ^{+1.2}_{-0\,\rm low}$
	RFXCONV	$Fe_{\rm abund}$ (Solar)	$1.29\ ^{+0.16}_{-0.16}$
	RFXCONV	log ξ	$2.57\ ^{+0.12}_{-0.09}$
	CONST	(MOS1)	$0.996\ ^{+0.008}_{-0.008}$
	CONST	(MOS2)	$1.000\ ^{+0.008}_{-0.008}$

0.3–1 keV band more significantly than in the CompTT-SE model. The LF lag spectrum favours a separate variable component dominating the soft excess such as in the CompTT-SE model.

A full spectral-timing modelling should consider all properties including the PSD, rms, covariance, coherence and lag spectra, and treat the variability propagation between different spectral components self-consistently. Gardner & Done (2014) performed this study for PG 1244+026. Their results also support the spectral decomposition of the CompTT-SE model, and indicate a weak reflection component in the soft X-ray region (similar as in Fig. 5b) which is mainly required by the HF soft X-ray lag detected in PG 1244+026. Considering the spectral similarity between PG 1244+026 and RX J0439.6−5311, we speculate that similar results could be obtained for RX J0439.6−5311 using the same analysis, but this is beyond the scope of this paper.

7 DISCUSSION

7.1 Origin of the soft excess in RX J0439.6−5311

The time-averaged X-ray spectra are degenerate to both Comptonization and reflection dominated models. But the frequency-dependent rms and covariance spectra clearly suggest that the soft excess in RX J0439.6−5311 is dominated by a separate component with strong LF variability, while the hard X-ray component contains stronger HF variability. The covariance spectra also indicates a weak non-variable component in the soft excess which is consistent with an origin in the inner disc. Moreover, the HF covariance spectra suggest that the seed photons for the hard X-ray Comptonization in the hot corona should have a higher temperature than the inner accretion disc, and so are more likely to come from the soft X-ray Comptonization region. These results clearly favour the CompTT-SE model. Then our time-lag analysis shows that in the LF band the soft X-rays lead the hard by ~ 4 ks and the lag spectrum has a broad profile in the hard X-ray band, which is most plausibly modelled as the propagation lag in the CompTT-SE model.

We note that our results are also consistent with the study of another example of a high mass accretion rate 'simple' NLS1 PG 1244+026 (J13; Alston et al. 2014a; Gardner & Done 2014). Although PG 1244+026 is radio-quiet, it does have some weak radio emission, so a contribution from the jet component was proposed as the origin of its soft X-ray excess (Kara et al. 2014). However, RX J0439.6−5311 has not been detected in any radio surveys, including the Parkes-MIT-NRAO (PMN) survey (Wright et al. 1994). This indicates that its radio emission is below the PMN's detection limit of $\lesssim$50 mJy at 4.85 GHz, implying $L_{4.85\rm GHz} < 4 \times 10^{41}$ erg s^{-1}. Compared to its optical flux of $L_{5100\text{Å}} = 2 \times 10^{44}$ erg s^{-1} (Grupe et al. 2004), we can conclude that RX J0439.6−5311 has no significant radio emission. This makes a jet origin much less likely for the soft X-ray excess in RX J0439.6−5311, yet the spectrum clearly has many similarities to PG 1244+026. More compellingly, the jet origin for the soft excess completely fails to fit the LF lag spectra of Fig. 12.

Based on all the above results, we can conclude that the soft excess in RX J0439.6−5311 is most likely produced in an extended intermediate region between the inner thermal disc and the compact hard X-ray corona (see Fig. 14). The low temperature electrons in this intermediate region are optically thick to the Compton upscattering of photons from the inner thermal disc, thereby producing the soft excess. Shielding the inner thermal disc, this intermediate region then provides soft X-ray seed photons for the high temperature, optically thin electrons in the hot corona to produce the hard X-ray Comptonization emission. Part of the emission from the hard X-ray region also reaches the soft X-ray region and may even penetrate into the thermal disc region behind, which is then partially reprocessed (thermalized) at the temperature close to the soft excess and partially reflected as a weak reflection component, thereby causing the HF variability in the soft excess.

We emphasize that in this paper we mainly compared extreme and simplest models where either Comptonization or reflection dominates the soft excess. But it is possible to have several components contributing the X-ray emission simultaneously, such as thermal disc, Comptonization, reflection, weak jet (but RX J0439.6−5311 has no radio emission) with more complex geometries (e.g. patchy corona, Wilkins & Gallo 2015). Our Figs 5 and 14 already show an

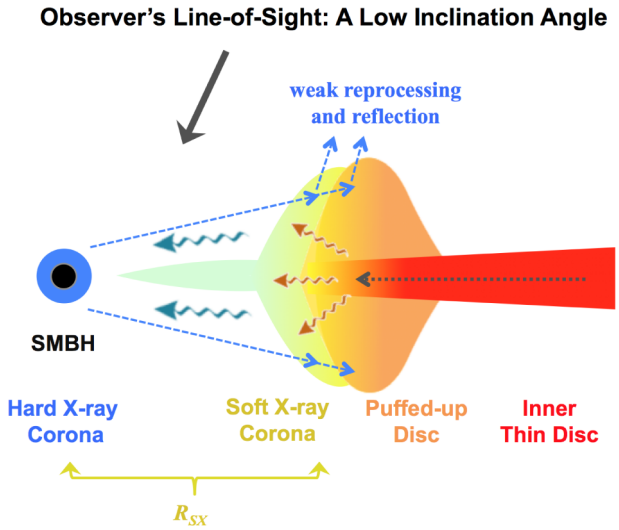

Figure 14. A schematic diagram of the inferred structure of the inner accretion flow in RX J0439.6−5311 and other super-Eddington 'simple' NLS1s. The soft X-ray corona is likely to be associated with the puffed-up inner disc region in these super-Eddington sources (see Section 7.1). R_{sx} is the distance between the extended soft X-ray corona and the compact hard X-ray corona estimated from the ∼ 4 ks time lag in RX J0439.6−5311, which is ∼80 R_g for $M = 10^7$ $M_\odot$ and ∼200R_g for $M = 4 \times 10^6$ $M_\odot$. A low inclination angle of 30° is adopted for RX J0439.6−5311 and is favoured by the clean line of sights in all the 'simple' NLS1s.

example of having both reflection and Comptonization in the spectra. What we report is that the CompTT-SE model can provide the simplest plausible explanation to all the spectral-timing properties of RX J0439.6−5311, while the other models cannot. Certainly we cannot rule out the possibility of having more complex geometry designs in order to make other scenarios work in RX J0439.6−5311, but such study is beyond the scope of this work, and we prefer the simplest solution.

7.2 Properties of the soft X-ray emitting region

The radial distance of this soft X-ray region to the black hole (i.e. R_{sx} in Fig. 14) is still unknown. But if the hard X-ray corona is fairly compact and close to the black hole (Galeev, Rosner & Vaiana 1979; Haardt & Maraschi 1991), and the soft X-ray region provides seed photons to the hard X-ray corona, then the 4 ks soft/hard X-ray time lag can be used to infer R_{sx}. For the single-epoch mass of 3.9×10^6 $M_\odot$ (Grupe et al. 2004), the light travel distance would imply $R_{sx} \simeq 200R_g$. This mass contains a factor of few uncertainty (e.g. Woo & Urry 2002), thus a black hole mass range of 10^6–10^7 $M_\odot$ would correspond to a R_{sx} range of 80–800 R_g. However, this R_{sx} is estimated using the speed of light, but it is also possible for some of the soft X-ray variability to propagate into the hard X-ray corona in the accretion flow (but we do not have a clear picture about it), so that this R_{sx} may be an upper limit for a fixed mass.

We also note that Grupe et al. (2004) reported $L/L_{Edd} = 12.9$ for their mass estimate, then $M = 10^6$ $M_\odot$ would imply $L/L_{Edd} = 50.3$, which is much higher than all other AGN known, so it is probably not likely for RX J0439.6−5311 to have such a small black hole mass (see our Paper-II for more detailed study), and so R_{sx} may not be as large as 800 R_g. Anyway, what the observation requires is an extended and geometrically thick soft X-ray region, sitting between the compact hard X-ray corona and the inner thermal disc. Since $R_{sx} \propto M^{-1}$, $\dot{m} \propto M^{-2}$ for an observed optical luminosity (Davis & Laor 2011), and the puffed-up disc radius (R_{pf}) is roughly proportional to $\dot{m}$ (Poutanen et al. 2007), reducing M will increase R_{sx} linearly, but increase R_{pf} quadratically, thus the condition of $R_{sx} \lesssim R_{pf}$ would be easier to satisfy.

We point out that the soft X-ray region is likely to be geometrically thick, which is because it needs to shield the hot corona from the thermal disc photons from several tens or hundreds of R_g away. Meanwhile, a so-called puffed-up disc region has been proposed to explain the weak optical/UV emission lines in weak-line quasars where high Eddington ratios are also observed (e.g. Madau 1988; Leighly 2004; Luo et al. 2015). Indeed, it is known that the accretion disc begins to deviate from a standard thin disc (Shakura & Sunyaev 1973) when the mass accretion rate approaches Eddington limit, in which case the disc becomes slim (e.g. Abramowicz et al. 1988; Wang & Netzer 2003), and is accompanied by significant advection and radiation driven disc wind (e.g. Ohsuga & Mineshige 2011; Jiang, Stone & Davis 2014; Hashizume et al. 2015; Sądowski & Narayan 2015; Hagino et al. 2016; DJ16). The shielding mechanism provided by the soft X-ray region is very similar to the function of the puffed-up inner disc region. In quasars of $M \gtrsim 10^8$ $M_\odot$, the puffed-up region needs to be high enough and very close to the X-ray corona (∼10 R_g, Luo et al. 2015 and references therein), but the disc in RX J0439.6−5311 must be much hotter because of its smaller black hole mass and higher mass accretion rate, and so the puffed-up region can be farther away, which enhances the possibility for the link between the soft X-ray region and the puffed-up inner disc region. We will report more detailed study on this in a subsequent paper on the multiwavelength spectrum of RX J0439.6−5311 (Paper-II).

8 CONCLUSIONS

In this paper, we report results of our X-ray analysis of an unobscured, highly super-Eddington QSO RX J0439.6−5311 based on a recent 133 ks *XMM–Newton* observation proposed by us. We show that the soft excess and hard X-rays of RX J0439.6−5311 exhibit different spectral-timing properties, which allows us to distinguish between Comptonization and reflection-dominated models for the spectral decomposition. We find that the reflection-dominated models can be ruled out for RX J0439.6−5311, and the X-ray emission from this source is most plausibly explained as the combination of the inner disc emission in the very soft X-ray band, the hard X-ray corona emission and the soft X-ray Comptonization emission dominating the soft excess, which is produced by a low temperature, optically thick electron population at several tens or hundreds of R_g radii (implied by the ∼4 ks soft X-ray leading the hard), which receives seed photons from the inner disc and also provides soft X-ray seed photons for the hard X-ray corona. This soft X-ray region is likely to be geometrically thick and associated with a puffed-up inner disc region.

While the general picture is becoming clearer, we note a significant difference between the HF rms and covariance spectra which implies that there is an additional uncorrelated fast variability component above 4 keV. The origin and properties of this component are not yet known, and it will require future observations with better S/N to constrain its properties.

ACKNOWLEDGEMENTS

We thank the anonymous referee for providing useful comments to improve the quality of the paper. CJ acknowledges the support by the Bundesministerium für Wirtschaft und Technologie/Deutsches

Zentrum für Luft- und Raumfahrt (BMWI/DLR, FKZ 50 OR 1408 and FKZ 50 OR 1604) and the Max Planck Society. CD and MJW acknowledge STFC funding under grant ST/L00075X/1. This work is based on a recent observation conducted by *XMM–Newton*, an European Space Agency (ESA) science mission with instruments and contributions directly funded by ESA Member States and the USA (National Aeronautics and Space Administration - NASA). This research has made use of the NASA/Infrared Processing & Analysis Center (IPAC) Extragalactic Database (NED) that is operated by the Jet Propulsion Laboratory, California Institute of Technology, under contract with the National Aeronautics and Space Administration.

REFERENCES

Abramowicz M. A., Czerny B., Lasota J. P., Szuszkiewicz E., 1988, ApJ, 332, 646
Ai Y. L., Yuan W., Zhou H. Y., Wang T. G., Zhang S. H., 2011, ApJ, 727, 31
Alston W. N., Done C., Vaughan S., 2014a, MNRAS, 439, 1548
Alston W. N., Markeviči_tė J., Kara E., Fabian A. C., Middleton M., 2014b, MNRAS, 445, L16
Arévalo P., M^{c}Hardy I. M., Markowitz A., Papadakis I. E., Turner T. J., Miller L., Reeves J., 2008, MNRAS, 387, 279
Arnaud K. A., 1996, in Jacoby G. H., Barnes J., eds, ASP Conf. Ser. Vol. 101, Astronomical Data Analysis Software and Systems V. Astron. Soc. Pac., San Francisco, p.17
Bendat J. S., Piersol A. G., 1986, Random Data, Analysis and Measurement Procedures. Wiley, New York
Bian W., Zhao Y., 2004, MNRAS, 347, 607
Boissay R. et al., 2014, A&A, 567, A44
Boller T., Brandt W. N., Fink H., 1996, A&A, 305, 53
Boroson T. A., 2002, ApJ, 565, 78
Boroson T. A., Green R. F., 1992, ApJS, 80, 109
Brandt W. N., Mathur S., Elvis M., 1997, MNRAS, 285, L25
Chainakun P., Young A. J., 2017, MNRAS, 465, 3965
Chiang C. Y., Walton D. J., Fabian A. C., Wilkins D. R., Gallo L. C., 2015, MNRAS, 446, 759
Crummy J., Fabian A. C., Gallo L., Ross R. R., 2006, ApJ, 365, 1067
Czerny B., Nikołajuk M., Różańska A., Dumont A.-M., Loska Z., Zycki P. T., 2003, A&A, 412, 317
Davis S. W., Laor A., 2011, ApJ, 728, 98
De Marco B., Ponti G., Cappi M., Dadina M., Uttley P., Cackett E. M., Fabian A. C., Miniutti G., 2013, MNRAS, 431, 2441
Done C., Jin C., 2016, MNRAS, 460, 1716
Done C., Nayakshin S., 2007, MNRAS, 377, L59
Done C., Davis S. W., Jin C., Blaes O., Ward M., 2012, MNRAS, 420, 1848
Done C., Jin C., Middleton M., Ward M., 2013, MNRAS, 434, 1955
Edelson R., Turner T. J., Pounds K., Vaughan S., Markowitz A., Marshall H., Dobbie P., Warwick R., 2002, ApJ, 568, 610
Fabian A. C., Miniutti G., 2005, preprint (arXiv:astro-ph/0507409)
Fabian A. C., Iwasawa K., Reynolds C. S., Young A. J., 2000, PASP, 112, 1145
Fabian A. C. et al., 2009, Nature, 459, 540
Fabian A. C. et al., 2013, MNRAS, 429, 2917
Fabian A. C., Parker M. L., Wilkins D. R., Miller J. M., Kara E., Reynolds C. S., Dauser T., 2014, MNRAS, 439, 2307
Freyberg M. J. et al., 2004, in Flanagan K. A., Siegmund O. H. W., eds, Proc. SPIE Conf. Ser. Vol. 5165, X-Ray and Gamma-Ray Instrumentation for Astronomy XIII. SPIE, Bellingham, p. 112
Galeev A. A., Rosner R., Vaiana G. S., 1979, ApJ, 229, 318
Gallo L. C., 2006, MNRAS, 368, 479
Gardner E., Done C., 2014, MNRAS, 442, 2456
Gardner E., Done C., 2015, MNRAS, 448, 2245
Gierliński M., Done C., 2004, MNRAS, 349, L7
Gierliński M., Done C., 2006, MNRAS, 371, L16
Gierliński M., Middleton M., Ward M., Done C., 2008, Nature, 455, 369
Grupe D., Wills B. J., Leighly K. M., Meusinger H., 2004, AJ, 127, 156
Grupe D., Komossa S., Leighly K. M., Page K. L., 2010, ApJS, 187, 64
Haardt F., Maraschi L., 1991, ApJ, 380, L51
Hagino K. Odaka H., Done C., Tomaru R., Watanabe S., Takahashi T., 2016, MNRAS, 461, 3954
Hashizume K., Ohsuga K., Kawashima T., Tanaka M., 2015, PASJ, 67, 58
Jansen F., Lumb D., Altieri B. et al., 2001, A&A, 365, L1
Jiang Y. F., Stone J. M., Davis S. W., 2014, ApJ, 796, 106
Jin C., Done C., Ward M., Gierliński M., Mullaney J., 2009, MNRAS, 398, L16
Jin C., Done C., Middleton M., Ward M., 2013, MNRAS, 436, 3173
Jin C., Done C., Ward M., 2016, MNRAS, 455, 691
Kalberla P. M. W., Burton W. B., Hartmann D., Arnal E. M., Bajaja E., Morras R., Pöppel W. G. L., 2005, A&A, 440, 775
Kara E., Fabian A. C., Cackett E. M., Steiner J. F., Uttley P., Wilkins D. R., Zoghbi A., 2013a, MNRAS, 428, 2795
Kara E., Fabian A. C., Cackett E. M., Miniutti G., Uttley P., 2013b, MNRAS, 430, 1408
Kara E., Fabian A. C., Cackett E. M., Uttley P., Wilkins D. R., Zoghbi A., 2013c, MNRAS, 434, 1129
Kara E., Cackett E. M., Fabian A. C., Reynolds C., Uttley P., 2014, MNRAS, 439, L26
Kara E., Alston W. N., Fabian A. C., Cackett E. M., Uttley P., Reynolds C. S., Zoghbi A., 2016, MNRAS, 462, 511
Kolehmainen M., Done C., Díaz Trigo M., 2011, MNRAS, 416, 311
Kotov O., Churazov E., Gilfanov M., 2001, MNRAS, 327, 799
Laor A., 1991, ApJ, 376, 90
Laor A., Fiore F., Elvis M., Wilkes B. J., McDowell J. C., 1997, ApJ, 477, 93
Leighly K. M., 1999, ApJS, 125, 317
Leighly K. M., 2004, ApJ, 611, 125
Lohfink A. M. et al., 2016, ApJ, 821, 11
Luo B. et al., 2015, ApJ, 805, 122
Lyubarskii Y. E., 1997, MNRAS, 292, 679
McHardy I. M., Arévalo P., Uttley P., Papadakis I. E., Summons D. P., Brinkmann W., Page M. J., 2007, MNRAS, 382, 985
Madau P., 1988, ApJ, 327, 116
Magdziarz P., Zdziarski A. A., 1995, MNRAS, 273, 837
Magdziarz P., Blaes O. M., Zdziarski A. A., Johnson W. N., Smith D. A., 1998, MNRAS, 301, 179
Markowitz A., Edelson R., Vaughan S., 2003, ApJ, 598, 935
Matt G. et al., 2014, MNRAS, 439, 3016
Mehdipour M. et al., 2011, A&A, 534, A39
Mehdipour M. et al., 2015, A&A, 575, A22
Middleton M., Done C., Ward M., Gierliński M., Schurch N., 2009, MNRAS, 394, 250
Middleton M., Uttley P., Done C., 2011, MNRAS, 417, 250
Miller L., Turner T. J., Reeves J. N., George I. M., Kraemer S. B., Wingert B., 2007, A&A, 463, 131
Miniutti G., Fabian A. C., 2004, MNRAS, 349, 1435
Miniutti G., Ponti G., Greene J. E., Ho L. C., Fabian A. C., Iwasawa K., 2009, MNRAS, 394, 443
Nandra K., George I. M., Mushotzky R. F., Turner T. J., Yaqoob T., 1997, ApJ, 477, 602
Noda H., Makishima K., Yamada S., Torii S., Sakurai S., Nakazawa K., 2011, PASJ, 63, 925
Nowak M. A., Wilms J., Vaughan B. A., Dove J. B., Begelman M. C., 1999, ApJ, 515, 726
Ohsuga K., Mineshige S., 2011, ApJ, 736, 2
Osterbrock D. E., Pogge R. W., 1985, ApJ, 297, 166
Porquet D., Reeves J. N., O'Brien P., Brinkmann W., 2004, A&A, 422, 85
Poutanen J., Lipunova G., Fabrika S., Butkevich A. G., Abolmasov P., 2007, MNRAS, 377, 1187
Poutanen J., Zdziarski A. A., Ibragimov A., 2008, MNRAS, 389, 1427

Reeves J., Done C., Pounds K., Terashima Y., Hayashida K., Anabuki N., Uchino M., Turner M., 2008, MNRAS, 385, L108
Ross R. R., Fabian A. C., 2005, MNRAS, 358, 211
Sądowski A., Narayan R., 2015, MNRAS, 453, 3213
Schurch N. J., Done C., 2007, MNRAS, 381, 1413
Shakura N. I., Sunyaev R. A., 1973, A&A, 24, 337
Sim S. A., Proga D., Miller L., Long K. S., Turner T. J., 2010, MNRAS, 408, 1396
Takeuchi S., Ohsuga K., Mineshige S., 2014, PASJ, 66, 48
Tatum M. M., Turner T. J., Sim S. A., Miller L., Reeves J. N., Patrick A. R., Long K. S., 2012, ApJ, 752, 94
Thomas H. C., Beuermann K., Reinsch K., Schwope A. D., Truemper J., Voges W., 1998, A&A, 335, 467
Timmer J., Koenig M., 1995, A&A, 300, 707
Titarchuk L., 1994, ApJ, 434, 570
Turner T. J., Miller L., Reeves J. N., Kraemer S. B., 2007, A&A, 475, 121
Uttley P., Cackett E. M., Fabian A. C., Kara E., Wilkins D. R., 2014, A&AR, 22, 72
Vaughan B. A., Nowak M. A., 1997, ApJ, 474, L43
Vaughan S., Fabian A. C., Nandra K., 2003a, MNRAS, 339, 1237
Vaughan S., Edelson R., Warwick R. S., Uttley P., 2003b, MNRAS, 345, 1271
Verner D. A., Ferland G. J., Korista K. T., Yakovlev D. G., 1996, ApJ, 465, 487
Wang J. M., Netzer H., 2003, A&A, 398, 927
Wilkins D. R., Gallo L. C., 2015, MNRAS, 449, 129
Wilkinson T., Uttley P., 2009, MNRAS, 397, 666
Wilms J., Allen A., McCray R., 2000, ApJ, 542, 914
Woo J. H., Urry C. M., 2002, ApJ, 579, 530
Wright A. E., Griffith M. R., Burke B. F., Ekers R. D., 1994, ApJS, 91, 111
Yaqoob T., Turner T. J., Tatum M. M., Trevor M., Scholtes A., 2016, MNRAS, 462, 4038
Zdziarski A. A., Johnson W. N., Magdziarz P., 1996, MNRAS, 283, 193
Zoghbi A., Fabian A. C., 2011, MNRAS, 418, 2642
Zoghbi A., Fabian A. C., Uttley P., Miniutti G., Gallo L. C., Reynolds C. S., Miller J. M., Ponti G., 2010, MNRAS, 401, 2419
Zoghbi A., Uttley P., Fabian A. C., 2011, MNRAS, 412, 59

APPENDIX A: FITTING RESULTS FOR THE REFLECTION MODELS AT 60° INCLINATION ANGLE

Table A1. Best-fitting parameters of the two fittings in Fig. A1 with the disc inclination angle fixed at 60°. These results can be compared to the best-fitting results in Table 1c,d. The upper and lower limits are for the 90 per cent confidence range. *low* (*up*) indicates the parameter's lower (upper) limit. DISKBB normalization is defined as $(R_{\rm in}/D_{10})^2\,cos\,\theta$, where $R_{\rm in}$ is the apparent inner disc radius in km, D_{10} is the source distance in units of 10 kpc, θ is the disc inclination angle. NTHCOMP and POWERLAW normalizations are given in units of photons $\rm keV^{-1}cm^{-2}s^{-1}$ at 1 keV.

Model	Component	Parameter	Value
REFLECTION	(Fig. A1a)	$\chi^2_\nu = 1285/1105 = 1.16$	
-DISC	TBNEW	$N_{\rm H}$ (10^{22} cm^{-2})	$0\ ^{+0.008}_{-0\,\rm low}$
	DISKBB	$T_{\rm in}$ (keV)	$0.105\ ^{+0.003}_{-0.004}$
	DISKBB	Norm	$2.53\ ^{+0.25}_{-0.14} \times 10^3$
	NTHCOMP	Γ	$2.69\ ^{+0.04}_{-0.04}$
	NTHCOMP	$kT_{\rm seed}$ (keV)	Tied to $kT_{\rm in}$
	NTHCOMP	Norm	$3.77\ ^{+0.57}_{-0.59} \times 10^{-4}$
	KDBLUR	Index	$5.67\ ^{+0.80}_{-0.53}$
	KDBLUR	$R_{\rm in}$ ($R_{\rm g}$)	$1.58\ ^{+0.12}_{-0.04}$
	RFXCONV	rel_refl ($\Omega/2\pi$)	$-0.17\ ^{+0.03}_{-0.17}$
	RFXCONV	$Fe_{\rm abund}$ (Solar)	$10.0\ ^{+0\,\rm up}_{-0.9}$
	RFXCONV	log ξ	$3.43\ ^{+0.05}_{-0.04}$
	CONST	(MOS1)	$0.993\ ^{+0.008}_{-0.008}$
	CONST	(MOS2)	$0.996\ ^{+0.009}_{-0.008}$
REFLECTION	(Fig. A1b)	$\chi^2_\nu = 1336/1105 = 1.21$	
-JET	TBNEW	$N_{\rm H}$ (10^{22} cm^{-2})	$0\ ^{+0.003}_{-0\,\rm low}$
	POWERLAW1	Γ	$3.44\ ^{+0.34}_{-0.07}$
	POWERLAW1	Norm	$3.21\ ^{+0.31}_{-1.46} \times 10^{-4}$
	POWERLAW2	Γ	$2.61\ ^{+0.04}_{-0.02}$
	POWERLAW2	Norm	$1.11\ ^{+0.18}_{-0.07} \times 10^{-4}$
	KDBLUR	Index	$10.0\ ^{+0\,\rm up}_{-0.14}$
	KDBLUR	$R_{\rm in}$ ($R_{\rm g}$)	$1.474\ ^{+0.025}_{-0.004}$
	RFXCONV	rel_refl ($\Omega/2\pi$)	$-10.0\ ^{+1.0}_{-0\,\rm low}$
	RFXCONV	$Fe_{\rm abund}$ (Solar)	$0.99\ ^{+0.07}_{-0.09}$
	RFXCONV	log ξ	$2.99\ ^{+0.05}_{-0.07}$
	CONST	(MOS1)	$0.968\ ^{+0.008}_{-0.007}$
	CONST	(MOS2)	$0.972\ ^{+0.007}_{-0.007}$

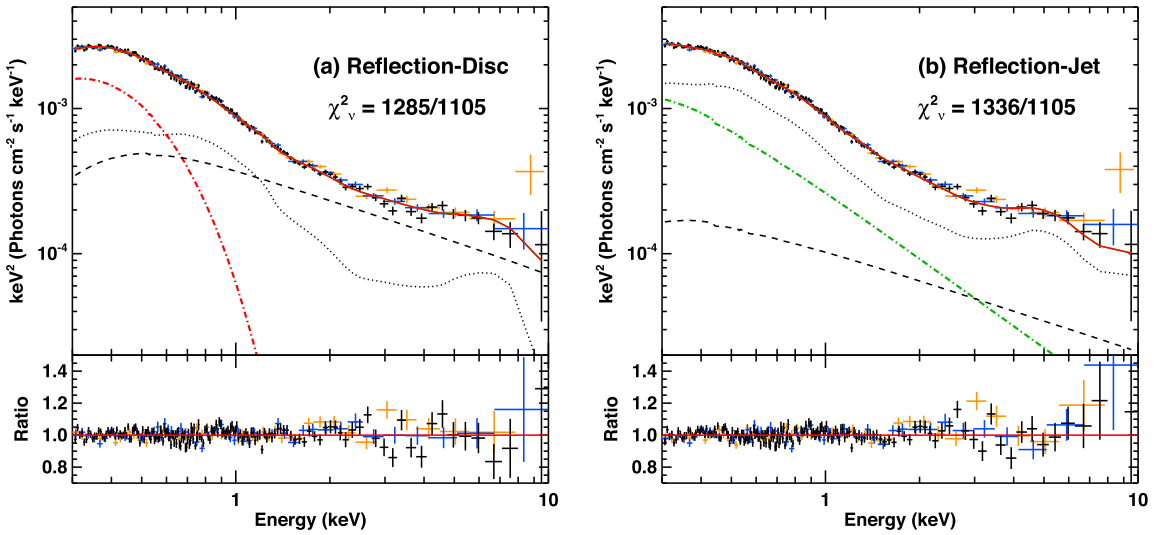

Figure A1. Best-fitting results for the two reflection models with the disc inclination angle fixed at 60°, which can be compared to the two fittings in Fig. 4(c,d) for 30°. The best-fitting parameters can be found in Table A1.

APPENDIX B: TIME-LAG AND COHERENCE SPECTRA WITH THE 2–10 KeV REFERENCE BAND

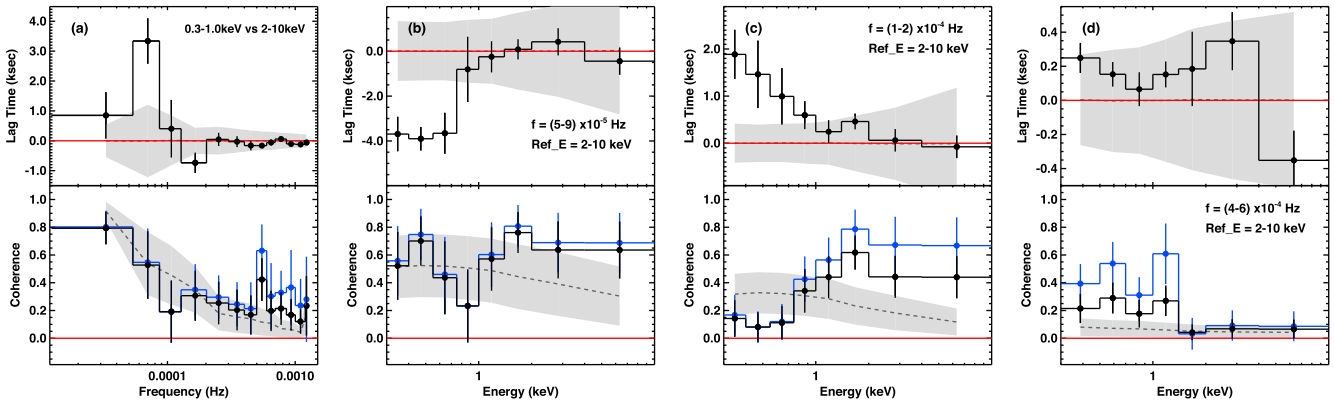

Figure B1. Similar to Fig. 11, but the simulation is based on the PSD of 0.3–1 keV (see Section 6).

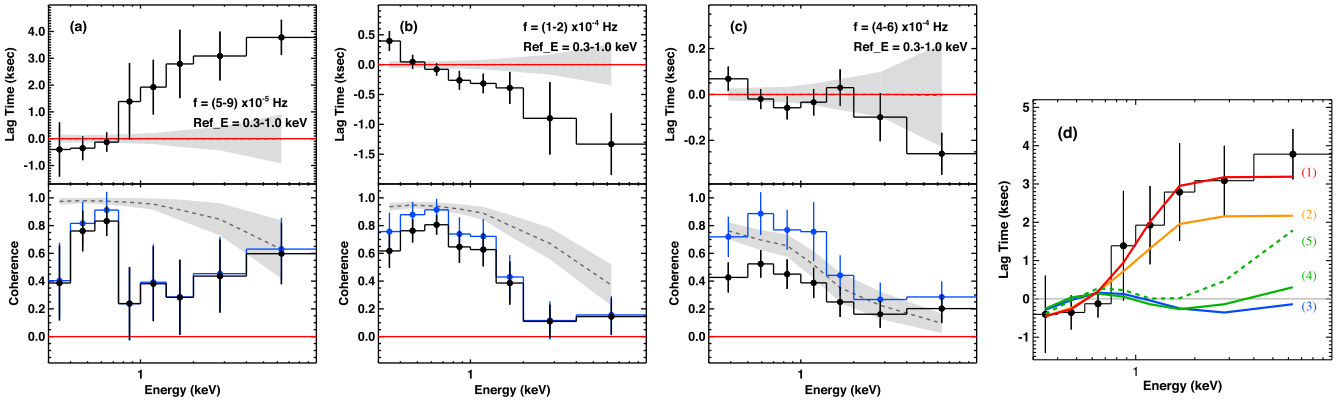

Figure B2. Panels a, b, c are similar to Fig. 11(b–d), and Panel d is similar to Fig. 12. But these results are based on the reference band of 0.3–1 keV.

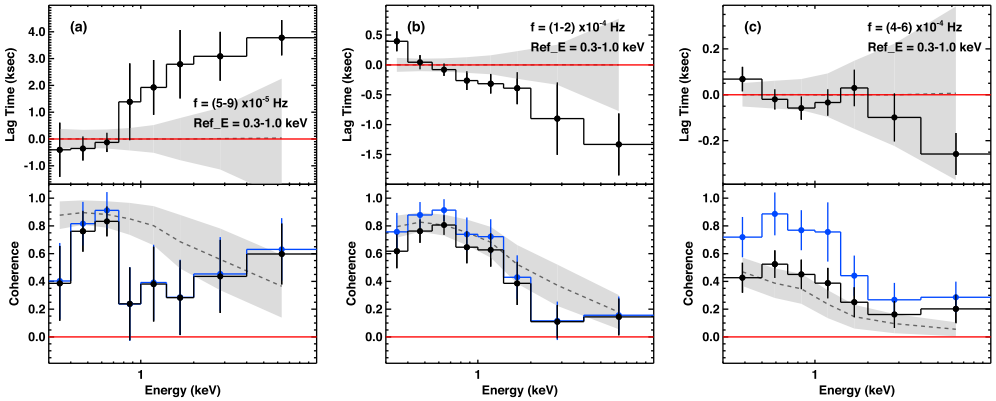

Figure B3. Similar to Fig. B2(a–c), but the simulation is based on the PSD of 0.3–1 keV.

This paper has been typeset from a TEX/LATEX file prepared by the author.